Diffusion and fluid interaction in Itrongay pegmatite (Madagascar): Evidence from in situ 40Ar/39Ar dating of gem-quality alkali feldspar and U Pb dating of protogenetic apatite inclusions

Daniil V. Popov, Richard A. Spikings, Stéphane Scaillet, Gary O'Sullivan, David M Chew, Eszter Badenszki, J. Stephen Daly, Théodore Razakamanana, Joshua H.F.L. Davies

Chemical Geology 556 (2020) 119841

Contents lists available at ScienceDirect

Chemical Geology

journal homepage: www.elsevier.com/locate/chemgeo

Diffusion and fluid interaction in Itrongay pegmatite (Madagascar): Evidence from in situ $^{40}Ar/^{39}Ar$ dating of gem-quality alkali feldspar and U–Pb dating of protogenetic apatite inclusions

Daniil V. Popov[a,*], Richard A. Spikings[a], Stéphane Scaillet[b], Gary O'Sullivan[c,d], David Chew[c,e], Eszter Badenszki[d,e], J. Stephen Daly[d,e], Théodore Razakamanana[f], Joshua H.F.L. Davies[a,g]

[a] Department of Earth Sciences, University of Geneva, 13 Rue des Maraichers, Geneva 1205, Switzerland
[b] Institut des Sciences de la Terre d'Orléans (ISTO), 1A rue de la Férollerie, 45071 Orléans Cedex 2, France
[c] Department of Geology, School of Natural Sciences, Trinity College Dublin, Dublin 2, Ireland
[d] UCD School of Earth Sciences, University College Dublin, Dublin 4, Ireland
[e] Irish Centre for Research in Applied Geosciences
[f] Département des Sciences de la Terre, Université de Toliara BP 185, Toliara 601, Madagascar
[g] Département des Sciences de la Terre et de l'Atmosphère, Université du Québec à Montréal, 201 avenue du Président Kennedy, H2X 3Y7 Montréal, QC, Canada

ARTICLE INFO

Editor: Balz Kamber

Keywords:
Itrongay
Madagascar
In situ
Alkali feldspar
$^{40}Ar/^{39}Ar$
Apatite
U-Pb
Dating
Thermochronology
Geochronology
Diffusion
Fluid
interaction.

ABSTRACT

Alkali feldspar $^{40}Ar/^{39}Ar$ and apatite U–Pb geochronological studies have typically invoked two mechanisms to account for apparent loss of radiogenic ^{40}Ar and $^{206\text{-}208}Pb$. Some studies have suggested that the radiogenic isotopes were lost by volume diffusion and used these dates to constrain temporal variations of rock temperatures; others have argued that the radiogenic isotopes were lost due to interaction with fluids and related these dates to chemical alteration. These two end-member interpretations have fundamentally different implications for tectonic models derived from geochronological data, and therefore it is important to reliably identify the principal mechanism for loss of radiogenic isotopes. Here, we revisit the mechanisms of ^{40}Ar loss in the famous gem-quality alkali feldspar from the Itrongay pegmatite in Madagascar. Previous studies have suggested that volume diffusion is the dominant mechanism of ^{40}Ar loss, providing key evidence to support the use of $^{40}Ar/^{39}Ar$ dating of alkali feldspar for thermochronology. We attempted to verify these results by obtaining time-temperature paths from petrologically characterised cogenetic feldspar and apatite from the Itrongay pegmatite and comparing them with each other. However, our results suggest that only a minor component in the variability of $^{40}Ar/^{39}Ar$ dates of Itrongay feldspar is related to the diffusive loss of ^{40}Ar, and that this loss was not compatible with the majority of previously proposed models, which hinders quantitative interpretations. The crystal studied here grew in five episodes related to the influx initially of co-existing dense SiO_2-rich solution and CO_2-dominated fluid (the first and supposedly the following two episodes) and subsequently of H_2O-rich fluid (supposedly the final two episodes). Much greater component in the variability of the acquired $^{40}Ar/^{39}Ar$ dates is interpreted to reflect the differences in the ages of these growth episodes, which we estimate to span from 477 Ma to 176 Ma (the first four episodes). Apatite inclusions in this crystal are interpreted to be xenocrysts derived from the country rocks of the Itrongay pegmatite. These yield older U–Pb dates than the estimated age of their host feldspar and have apparently experienced diffusive loss of $^{206,207}Pb$ prior to entrapment. Our $^{40}Ar/^{39}Ar$ results indicate that there is a lack of unambiguous evidence for diffusive loss of ^{40}Ar from alkali feldspar that can be readily interpreted for thermochronological purposes. However, in situ $^{40}Ar/^{39}Ar$ dating of alkali feldspar appears to be a promising tool for tracking fluid-flow events in the Earth's crust whose applicability is not restricted to sedimentary rocks. Our U–Pb results corroborate previous suggestions that U–Pb dating of apatite can be used for thermochronology.

* Corresponding author.
E-mail addresses: d.vs.popov@gmail.com, Daniil.Popov@unige.ch (D.V. Popov).

https://doi.org/10.1016/j.chemgeo.2020.119841
Received 23 April 2020; Received in revised form 3 August 2020; Accepted 24 August 2020
Available online 27 August 2020

1. Introduction

Many geological studies use isotopic dating of minerals for constraining the thermal histories of rocks. Time-temperature paths have been frequently inferred from $^{40}Ar/^{39}Ar$ data acquired by stepwise heating of alkali feldspar (e.g. Harrison and Lovera, 2014 and references therein) and increasingly more often using apatite U−Pb data (e.g. Paul et al., 2019 and references therein). Interpretations of these data assume that the loss of radiogenic ^{40}Ar from alkali feldspar and radiogenic $^{206\text{-}208}Pb$ from apatite occurs solely by volume diffusion before cooling below ~150–350 °C and ~ 350–550 °C, respectively. However, a growing number of studies suggest that the distributions of ^{40}Ar in alkali feldspar (Chafe et al., 2014; Parsons et al., 1999; Villa and Hanchar, 2013) and $^{206\text{-}208}Pb$ in apatite (Glorie et al., 2019; Kirkland et al., 2018) can be significantly altered by fluid-induced dissolution-reprecipitation at temperatures within or below the specified temperature windows. This can impair our ability to constrain the thermal histories of rocks using alkali feldspar $^{40}Ar/^{39}Ar$ and apatite U−Pb data. The aim of this study is to improve our understanding of whether and in which geologic settings we can find alkali feldspar and apatite that were not significantly affected by fluid-induced dissolution-reprecipitation and thus are suitable for thermochronology.

Here we focus on the mechanisms of ^{40}Ar loss from alkali feldspar, which have been intensively debated over the past 30 years. Some studies have used step-heating $^{40}Ar/^{39}Ar$ analysis of bulk grains to suggest that the dominant mechanism for ^{40}Ar redistribution is volume diffusion (Harrison and Lovera, 2014; Lovera et al., 2002, 1989). However, other studies indicate that alkali feldspar is usually affected by fluid-induced recrystallisation and suggested that this process is more likely to account for the date variations in the $^{40}Ar/^{39}Ar$ age spectra (Chafe et al., 2014; Parsons et al., 1999; Villa and Hanchar, 2013). Furthermore, crystals that have partially lost ^{40}Ar by either volume diffusion or fluid-induced recrystallisation can yield indistinguishable step-heating $^{40}Ar/^{39}Ar$ data (Popov and Spikings, 2020), while laboratory heating can significantly alter the inventory of fast diffusion pathways (Popov et al., 2020). These factors make it problematic to assess the role of volume diffusion in resetting ^{40}Ar concentrations solely by using step-heating $^{40}Ar/^{39}Ar$ analysis. Only a few studies have used in situ techniques to obtain Ar isotope data from alkali feldspar from non-sedimentary rocks, and only one of them documented ^{40}Ar concentration gradients consistent with diffusive loss. Flude et al. (2014) report that in situ $^{40}Ar/^{39}Ar$ dates of a gem-quality alkali feldspar crystal from the Itrongay pegmatite (Madagascar) gradually increase from the rim towards the core. They were able to reproduce the observed $^{40}Ar/^{39}Ar$ date variations by modelling diffusive loss of ^{40}Ar that occurred while this crystal cooled following a simplified version of the regional time-temperature path. Flude et al. (2014) applied diffusion parameters that were obtained by Wartho et al. (1999) for other crystals of Itrongay feldspar, which led them to suggest that accurate thermal histories of rocks can be recovered from in situ or step-heating $^{40}Ar/^{39}Ar$ data using sample-specific experimentally-derived diffusion parameters. Our work is an attempt to verify these results.

Gem-quality crystals of Itrongay feldspar are considered to behave largely as single grain-scale diffusion domains both over geological time and in laboratory experiments (Arnaud and Kelley, 1997; Cassata and Renne, 2013; Flude et al., 2014; Lovera et al., 2015; Wartho et al., 1999). Given that these crystals can reach several cm in the shortest dimension, this suggests that their closure temperature with respect to diffusive loss of ^{40}Ar should fall within the temperature range that is usually constrained using the apatite U−Pb thermochronometer (i.e. ~350–550 °C; Cherniak, 2010a; Chamberlain and Bowring, 2001; Cochrane et al., 2014; Paul et al., 2019). The equation of Dodson (1973) yields a closure temperature of 441 °C for a spherical alkali feldspar crystal with a diameter of 1 cm, a cooling a rate of 20 °C/Ma, and using the diffusion properties defined by the low-temperature Arrhenius relationship from Wartho et al. (1999). This potential overlap between the closure intervals for Ar in alkali feldspar and Pb in apatite thus provides an opportunity to directly compare thermochronological constraints obtained using these systems and thereby verify their accuracy. Therefore, our work was set out to (i) find and characterise cogenetic gem-quality alkali feldspar and apatite from the Itrongay pegmatite, (ii) date them using in situ $^{40}Ar/^{39}Ar$ and U−Pb methods, respectively, and (iii) derive an independent time-temperature path for each of them and compare these paths. However, while we were able to find a crystal of Itrongay feldspar that contains inclusions of apatite, they could not be used for thermal history reconstruction. Petrological and geochronological evidence suggests that the feldspar crystal records a protracted history of interaction with fluids with only minor diffusive loss of ^{40}Ar that could not be quantified, while the apatite inclusions are xenocrysts that predate this feldspar crystal by at least several tens of millions of years.

2. Previous work

2.1. Previous studies of Itrongay feldspar

Itrongay feldspar is a vague term that is applied to gem-quality alkali feldspar crystals that are reportedly derived from several pegmatitic bodies scattered over a ~5 × 20 km area in southern Madagascar. Previous studies of Itrongay feldspar do not report sampling coordinates, probably because they used crystals that were bought from brokers and cannot be traced back to a specific location (e.g. Nägler and Villa, 2000). It is important to keep this in mind because different crystals may have experienced different geologic histories, and any observation made for one crystal is not necessarily valid for others. Typically, Itrongay feldspar is yellow transparent gem-quality orthoclase to low sanidine with high concentrations of K (K > 0.9 apfu, frequently > 0.94 apfu) and Fe (up to 0.11 apfu; Arnaud and Kelley, 1997; Nyfeler et al., 1998; Wartho et al., 1999; Simmons and Falster, 2002; Ackermann et al., 2004; Parsons and Lee, 2005). Transmission electron microscopy observations of Wartho et al. (1999) and Parsons and Lee (2005) showed that it has a nm-scale tweed texture and ~15–25 nm wide inclusions of an unidentified mineral. Parsons and Lee (2005) report exsolution lamellae of Na-rich feldspar with thicknesses of up to 10 nm and lengths of up to 500 nm, which could form at very low temperature (potentially below 200 °C). Experimental studies on Ar diffusion in Itrongay feldspar have obtained non-linear Arrhenius arrays using both step-heating of bulk grains and in situ analysis of partially outgassed grains (Arnaud and Kelley, 1997; Cassata and Renne, 2013; Wartho et al., 1999). Several phenomena have been invoked to explain these non-linear Arrhenius arrays, which include structural transitions (Cassata and Renne, 2013; Wartho et al., 1999), changes in vacancy-specific mechanisms of diffusion (Wartho et al., 1999), the presence of fast pathways for Ar diffusion (Arnaud and Kelley, 1997; see also Baxter, 2010) and the presence of variably-sized intra-grain diffusion domains (Lovera et al., 2015). Nevertheless, it is generally considered that the effective diffusion length of Itrongay feldspar grains is well approximated by their half-width (Arnaud and Kelley, 1997; Cassata and Renne, 2013; Wartho et al., 1999; consider also that the size of the largest domain in Lovera et al., 2015, is assumed to be equal to the size of the analysed grain). Previous step-heating $^{40}Ar/^{39}Ar$ analyses of Itrongay feldspar gave plateau dates of 435 ± 8 Ma (Arnaud and Kelley, 1997; 2σ errors are shown throughout) and 461 ± 6 Ma (Nägler and Villa, 2000), while previous in situ $^{40}Ar/^{39}Ar$ dates vary between 416 ± 3 Ma and 474 ± 5 Ma (Flude et al., 2014). Nägler and Villa (2000) obtained by bulk-grain analysis a K−Ca isochron date of 477 ± 2 Ma. These variations in isotopic dates have been attributed to the diffusive loss of ^{40}Ar (Flude et al., 2014; Nägler and Villa, 2000).

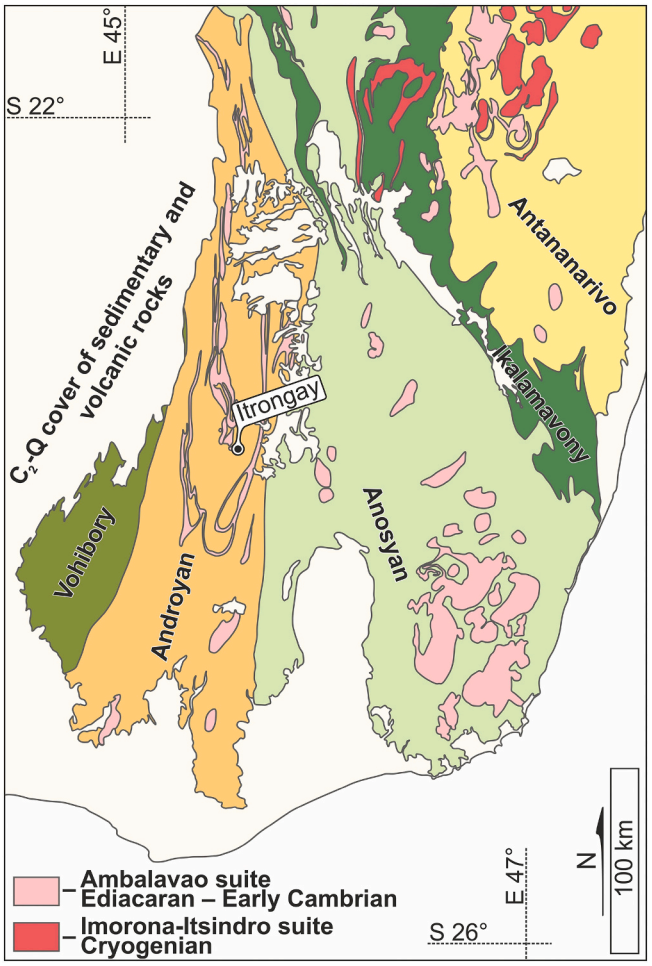

Fig. 1. Geological terrane map showing the relationships between the Vohibory, Androyan, Anosyan, Ikalamavony and Antananarivo domains in the south of Madagascar (adopted from Roig et al., 2012). Ambalavao and Imorona-Itsindro suites are suites of largely metamorphosed intrusive rocks. The label "Itrongay" shows the location of the ~5 × 20 km field of "pegmatites dites d'Itrongay" from the maps of Savornin (1932, 1933). We sampled near the southwestern boundary of this field (see in Section 4.1 for details).

2.2. Geological background

Itrongay feldspar is reportedly derived from several pegmatite bodies located in the south of Madagascar within the Androyan domain (Fig. 1; proximal to the villages of Beapombo II). High-grade metamorphic and magmatic rocks of the Androyan domain formed in the Ediacaran to early Cambrian during the accretion of East and West Gondwana and associated intervening terranes (Collins et al., 2012; de Wit et al., 2001; Tucker et al., 2014). The peak metamorphic conditions within this domain reached 7–9 kbar and 800–950 °C, and some rocks provide evidence for retrogression at 3–5 kbar and 650–730 °C (Markl et al., 2000; Tucker et al., 2014). The majority of studies suggest that this period of high-temperature metamorphism and associated magmatism terminated at ~520–500 Ma, which corresponds to the youngest zircon, monazite and titanite U-(Th)-Pb dates obtained for many rocks from the Vohibory, Androyan and Anosyan domains of southern Madagascar (Collins, 2006; Collins et al., 2012; de Wit et al., 2001; Holder et al., 2018; Holder and Hacker, 2019; Horton et al., 2016; Jöns and Schenk, 2011; Martelat et al., 2000; Tucker et al., 2014). A longer duration of high-temperature metamorphism, lasting until ~450–420 Ma, was proposed by Berger et al. (2006) and Giese et al. (2011) to account for monazite U-Th-Pb dates of ~420–500 Ma that were obtained from some retrogressed rocks. However, other studies suggest that similarly young U-(Th)-Pb dates of monazite (Fernandez et al., 2003; Grégoire et al., 2009; Martelat et al., 2000) and titanite (Holder and Hacker, 2019) and $^{40}Ar/^{39}Ar$ dates of micas (Fernandez et al., 2003) are a result of fluid-induced recrystallisation at ≲400 °C. The majority of the published U−Pb dates of titanite and rutile are older than 500 Ma and 480 Ma, respectively (de Wit et al., 2001; Emmel et al., 2008; Holder and Hacker, 2019), step-heating $^{40}Ar/^{39}Ar$ dates of biotite and phlogopite vary between ~450–500 Ma (Emmel et al., 2008; Martin et al., 2014; Montel et al., 2018), a (U−Th)/He date of ~510–530 Ma was obtained for a cm-scale, gem-quality crystal of monazite (Montel et al., 2018), and fission-track dates of ~275–380 Ma have been reported for titanite (Emmel et al., 2004). This evidence was used to suggest that the rock temperatures in southern Madagascar decreased below ~400 °C between ~530–490 Ma (de Wit et al., 2001; Emmel et al., 2008; Holder and Hacker, 2019) and below ~300 °C between ~500–300 Ma (Emmel et al., 2008, 2004; Holder and Hacker, 2019; Montel et al., 2018), which is incompatible with the persistence of high-temperature metamorphism between 500 and 420 Ma. Previously reported apatite fission-track and (U−Th)/He dates vary between 68 and 372 Ma and 85–197 Ma, respectively, which was interpreted to reflect cooling of the rocks through ~60–150 °C between ~400–200 Ma, with some local reheating to ~80 °C due to Cretaceous and Cenozoic volcanism (Emmel et al., 2012, 2008, 2004; Seward et al., 2004).

3. Methods

Non-destructive characterisation of the studied Itrongay feldspar crystal and apatite inclusions within it was carried out using equipment housed at the University of Geneva. Backscattered electron (BSE) imaging and semiquantitative analyses via energy-dispersive X-ray spectroscopy (EDS) were acquired using a JEOL JSM7001F scanning electron microscope equipped with an EDS JED2300 analyser. Optical cathodoluminescence (CL) images were acquired using an ERI-MRTech stage. Raman spectra were acquired using a HORIBA LabRAM spectrometer and interpreted using the RRUFF database (Lafuente et al., 2015), which provided the reference spectra for pyroxene, carbonate, apatite and baddeleyite, along with the studies of Beyssac et al. (2002), Frezzotti et al. (2012), Cicconi and Neuville (2019) and Curtis et al. (2019), which provided the reference spectra for graphite, CO_2, SiO_2-rich glass and opal, respectively. Selected Raman spectra of opal are given in Supplementary Tables (sheet Raman spectra of opal).

In situ $^{40}Ar/^{39}Ar$ dates were obtained from a ~0.5 mm thick crystal slice going through the centre of the Itrongay feldspar crystal. The slice was irradiated along with Fish Canyon Tuff sanidine for 13 h without Cd shielding (ICIT) in the F12 position of the TRIGA reactor at the Oregon State University. The slice was fixed horizontally during the irradiation to minimise potential variations in the neutron flux across it, and four monitors were fixed around the slice to seek lateral variations in the neutron flux, although none were detectable. In situ $^{40}Ar/^{39}Ar$ data were obtained at the Institut des Sciences de la Terre d'Orléans with the use of a Teledyne Cetac LSX-213 G2 213 nm Nd:YAG laser ablation system. Each single analysis comprises gas released either from 12 spots with a diameter of 20 μm or 4 spots with a diameter of 50 μm. The spots defined a straight line that was orthogonal to the chosen general direction of analysis (usually parallel to the nearest crystal boundary). The released gas was purified for 6 min using a liquid N_2 cold trap and two hot SAES GP50 getters and two Ta filaments held at 1500 °C. $^{36,37,38,39,40}Ar$ along with ^{35}Cl were measured by peak jumping in 10 cycles of 70-second duration using an electron multiplier detector of a Thermo Fisher Helix SFT mass spectrometer. Peak intensity data were reduced following the procedures of Scaillet (2000). Fish Canyon Tuff sanidine monitors were analysed at the University of Geneva. Each monitor was degassed using a CO_2 infrared laser, and the released gas was purified for 6.5 min using a cold trap (−130 °C) and hot SAES AP10 and GP50 (ST101) getters. $^{36,37,38,39,40}Ar$ isotopes were measured

in 12 cycles of 1-minute integrations using a GV Instruments Argus V mass spectrometer fitted with four 10^{12} Ω Faraday collectors for ^{36,37,38,39}Ar, and one 10^{11} Ω Faraday collector for ^{40}Ar. Peak intensity data were reduced using ArArCALC V2.4 (Koppers, 2002). All of our calculations were made using the ^{40}K decay constants of $\lambda_{e.c.} = 0.581 \times 10^{-10}\ yr^{-1}$ and $\lambda_{\beta^-} = 4.962 \times 10^{-10}\ yr^{-1}$ (Steiger and Jäger, 1977). Fish Canyon Tuff sanidine was used as a neutron flux monitor with an age of 28.201 ± 0.046 Ma (Kuiper et al., 2008). Mass discrimination factors were determined by analysing air with $^{40}Ar/^{36}Ar = 295.5$ (Steiger and Jäger, 1977). $^{40}Ar/^{39}Ar$ data are provided in Supplementary Tables (sheet Ar−Ar dates).

Semiquantitative trace element maps of apatite were obtained by laser ablation inductively coupled plasma mass spectrometry (LA-ICPMS) at Trinity College Dublin. We used a Photon Machines Analyte Excite 193 nm ArF excimer laser ablation system with a HelEx 2-volume ablation cell coupled to an Agilent 7900 quadrupole mass spectrometer to measure ^{44}Ca, ^{55}Mn, ^{57}Fe, ^{88}Sr, ^{89}Y, ^{90}Zr, ^{137}Ba, ^{139}La, ^{206}Pb, ^{232}Th, ^{238}U by peak jumping. Apatite was analysed by ablating lines with a 7 μm diameter circular spot at a scan speed of 15 μm/s. The acquired mass spectrometry data were reduced in Iolite 2.5 (Paton et al., 2011) using the data reduction scheme trace_element_image, option semi_quantitative. In situ U−Pb dating of apatite was done by laser ablation multiple collector inductively coupled plasma mass spectrometry (LA-MC-ICPMS) at the National Centre for Isotope Geochemistry at University College Dublin. We used a Teledyne Cetac Analyte G2 193 nm ArF excimer laser ablation system with a HelEx II 2-volume ablation cell coupled to a Thermo Fisher Neptune mass spectrometer to simultaneously measure ^{238}U, ^{207}Pb, ^{206}Pb on separate electron multiplier detectors (we also monitored ^{232}Th, ^{202}Hg, ^{204}Pb, ^{208}Pb and ^{235}U, but these were not used in the U−Pb date calculations). Apatite was analysed by ablating 20 × 20 μm square spots. The acquired data were reduced using in-house MS Excel-based software that closely reproduces LAMTRACE (Jackson, 2008) and utilises the ratio-of-the-mean-intensities method of correction for U−Pb fractionation (Ulianov et al., 2012). The initial functionality of LAMTRACE was extended by implementing the ^{207}Pb-based algorithm for U−Pb fractionation correction using standards with variable quantities of common Pb (Chew et al., 2014). McClure Mountain apatite (Chew et al., 2014; Schoene and Bowring, 2006) was used as a primary standard, while Emerald Lake apatite and Durango apatite (Chew et al., 2011) were used as secondary standards. Common Pb correction was made using the ^{207}Pb-correction method (Chew et al., 2011) assuming a common Pb composition predicted by the model of Stacey and Kramers (1975). U−Pb data are provided in Supplementary Tables (sheet U−Pb dates).

4. Results

4.1. Sampling and field observations

The Itrongay feldspar crystal that we used in our study was picked from the ground in the vicinity of Beapombo II village (approximate sampling location is S 23°35′33" E 45°34'06"). Due to poor bedrock exposure, we only have fragmentary information on its geologic context, which is largely based on the observation of rock fragments scattered around abandoned pits. We observed the following seven rock types (1–7): (1–2) quartz-feldspar rocks that are sometimes interlayered with pyroxene-phlogopite rocks (Fig. 2B, C), (3) pyroxene-feldspar rock (Fig. 2D), (4) friable rock that consists of phlogopite and presumably kaolinite (Fig. 2E), (5) variably deformed and altered pegmatitic rocks that only consist of green feldspar (Fig. 2F, G), (6) sometimes brecciated pegmatitic rocks that consist of smoky quartz and green feldspar (Fig. 2H, I), and (7) very coarse-grained rocks that consist of pyroxene, feldspar, quartz and titanite (Fig. 2J, K). Some of the brecciated pegmatitic rocks are cemented with opal-CT (identified using Raman spectroscopy). One of the samples of brecciated quartz-feldspar pegmatitic rock contained a large brecciated amphibole crystal. We interpret the pyroxene-phlogopite, quartz-feldspar and pyroxene-feldspar rocks (types 1–3) to be host rocks that were intruded by one or several pegmatitic bodies, which have feldspathic flanks (type 5) and quartzofeldspathic cores (type 6). The friable rock with phlogopite (type 4) occurs at the contact between the pyroxene-feldspar country rock and the deformed pegmatitic rock that consists only of feldspar, suggesting that it is either an altered aplitic rim of a pegmatitic body or a hydrothermally reworked fault zone. The relationship between these rocks and the coarse-grained rocks consisting of pyroxene, feldspar, quartz and titanite (type 7) is unclear.

We observed a variety of gem-quality feldspar grains that ranged in colour from green to yellow. The green and greenish yellow grains never form euhedral crystals and represent fresh fragments of large feldspar crystals from the abovementioned pegmatitic rocks (greenish yellow grains tend to occur with smoky quartz in brecciated samples; Fig. 2G-I). In contrast, the yellow grains sometimes form euhedral crystals, which typically have etched surfaces and in some cases are overgrown by a thin layer of whitish turbid felspar (Fig. 3A, B). These grains fit the description of typical Itrongay feldspar provided in Section 2.1 and will be referred to by this term for the rest of this work. Most of these grains were picked from the ground. We have found only one rock sample containing yellow gem-quality felspar, which is a deformed feldspar-dominated pegmatitic rock that was collected at the contact with pyroxene-feldspar country rock. In this sample, two yellow feldspar fragments, which once were part of a larger crystal, are surrounded by a matrix of brecciated and altered green feldspar (Fig. 2F).

4.2. Feldspar characterisation and $^{40}Ar/^{39}Ar$ dating

We have studied one euhedral crystal of Itrongay feldspar, which appears turbid when viewed from the side but has a transparent and gem-quality interior (Fig. 3A, B). The apparent turbidity is related to natural etching and a thin overgrowth layer of turbid feldspar. This crystal contains a variety of inclusions, which are unevenly distributed. Three growth zones can be distinguished based on the assemblage and the morphology of the inclusions. In the core (zone 1) this crystal contains inclusions of liquid CO_2, amorphous SiO_2, carbonates, apatite, pyroxene and baddeleyite (Fig. 3C-P). The majority of liquid CO_2 inclusions and amorphous SiO_2 inclusions have well-developed negative crystal shapes (Fig. 3C, D, F, H). Liquid CO_2 inclusions exsolve into liquid and gas after a few minutes in a regular refrigerator (Fig. 3L, M), suggesting that their homogenisation temperature is only slightly lower than room temperature (20–25 °C). Similar CO_2 inclusions were also reported from Itrongay feldspar by Touret (1974, 1977), and the inclusion shown in Touret (1977) consists of liquid and gas at room temperature. Amorphous SiO_2 inclusions yield Raman spectra (Fig. 3E) that are typical of opal-CT (Curtis et al., 2019). These can be distinguished from Raman spectra of SiO_2-rich glasses (Cicconi and Neuville, 2019) because the low-frequency band is shifted to < 400 cm^{-1} (specifically to ~350 cm^{-1}) and the high-frequency band at ~900–1400 cm^{-1} is absent. Three types of carbonate inclusions are present. Two of these are opaque isometric inclusions with well-developed crystal shapes and characteristic peaks in Raman spectra at different positions (Carb1 in Fig. 3C, D, and Carb3 in Fig. 3O). Their opaqueness is probably related to natural etching prior to entrapment (note the rough surface of Carb1 in Fig. 3D). Carbonate inclusions of the third type are transparent and have irregular shapes, and they are usually co-trapped with pyroxene and/or liquid CO_2 (Carb 2 in Fig. 3F, L, M). Apatite inclusions are isometric and have no pronounced faceting (Fig. 3F, H, J, O). Smaller apatite inclusions are transparent and are sometimes co-trapped with liquid CO_2 or amorphous SiO_2 (Ap1 in Fig. 3F, H, J). Larger apatite inclusions appear turbid when viewing from the side, perhaps due to natural etching prior to their entrapment, and they are occasionally co-trapped with opaque carbonate (Ap2 in Fig. 3O) or sub-isometric pyroxene. Pyroxene inclusions are sometimes well-faceted and generally have a needle-like or even hair-like

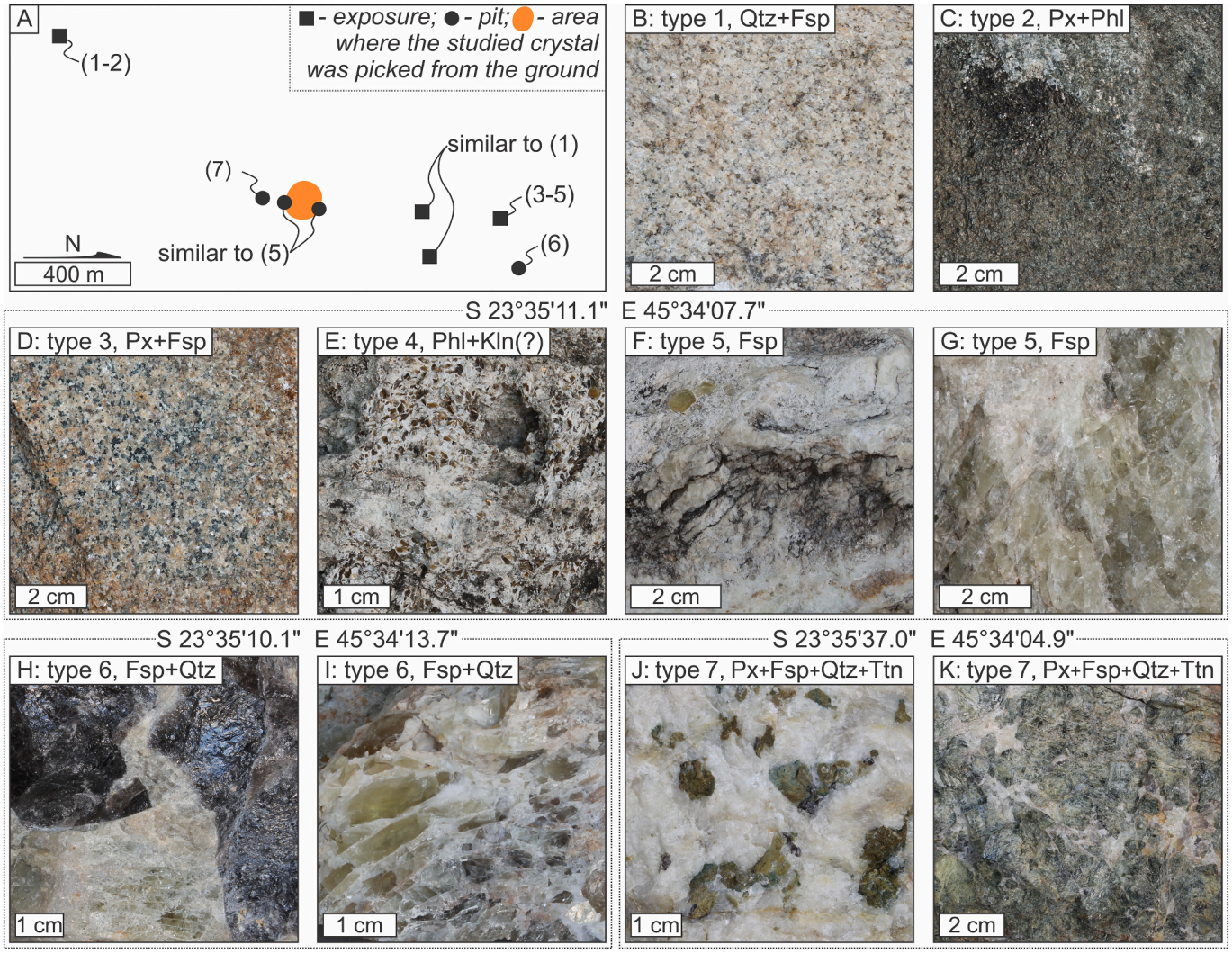

Fig. 2. Sampled rock types and their spatial distribution. A: schematic map showing relative position of outcrops and pits where we made our observations. B-K: photos of all the rock types that we observed. See text for descriptions of rocks. Qtz – quartz, Fsp – feldspar, Px – pyroxene, Phl – phlogopite, Kln – kaolinite, Ttn – titanite. White matter between greenish yellow feldspar clasts in Fig. 2I is opal-CT. For interpretation of the references to colour in this figure legend, the reader is referred to the web version of this article.

morphology (Fig. 3L, M), although platy and sub-isometric crystals were also observed. According to our semiquantitative EDS analyses, the needle-like crystals are inclusions of Fe-rich diopside with Fe/Mg ratios approaching 1 (in at. %). Very small baddeleyite crystals were co-trapped with an apatite crystal and amorphous SiO_2 (Fig. 3H). Zone 1 is followed by zone 2, which comprises the outer $\lesssim$ 1 mm of gem-quality feldspar and hosts very scarce and small inclusions. The inclusions are slightly elongated or more often isometric pyroxene crystals with irregular morphologies, which are generally co-trapped with other phases, including graphite, CO_2, apatite and an unidentified phase that has strong luminescence (Figs. 3Q-T). Zone 2 is followed by zone 3, which comprises the outer $\lesssim$ 0.1 mm layer of turbid feldspar and contains abundant tiny inclusions that cause the turbidity (Fig. 3U; nanopores with fluid?).

CL and BSE imaging also showed that the studied crystal has complex internal zoning, which partly correlates with the distribution of inclusions and the variation in turbidity. The same three major zones can be distinguished in the CL image of this crystal (Fig. 4A), which includes a deep blue core with very weak CL (zone 1), a light blue intermediate zone with bright CL (zone 2) and a deep blue outer rim with very weak CL (zone 3). The boundary between zones 1 and 2 is irregular, wavy and is marked by a change in the assemblage of inclusions, as described above. Feldspar remains optically coherent across this boundary, and zones 1 and 2 become simultaneously extinct in cross-polarised light. The boundary between zones 2 and 3 is irregular, wavy in some places and straight in others, and zone 3 is turbid and has a different extinction angle to zones 1 and 2. These three major zones can also be distinguished in the high-contrast BSE image (Fig. 4B), where the inner boundary of zone 2 is marked by a prominent dark wavy stripe, while zone 3 is considerably darker than the rest of the crystal. However, additional complexity is observed within zone 2, which is divided by a less prominent dark wavy stripe into two subzones, an inner subzone 2a and an outer subzone 2b. The two dark stripes sometimes merge, so that subzone 2a pinches out. Lastly, higher magnification BSE images (Fig. 4D) reveal that zone 3 also comprises two subzones, which are a thicker and darker inner subzone 3a and a thinner and brighter outer subzone 3b. The relationships between all of the (sub)zones are summarised in Fig. 4E. Our semiquantitative EDS analyses suggest that the composition of the studied crystal varies from zone to zone. Exceptionally high Fe concentrations (a few wt%) were only observed in zone 1. The Na/K ratio remains constant across zones 1 and 2, where the Na concentration is very low. No Na was detected in zone 3, and subzone 3b has a very high concentration of Ba (several wt %). Notably, despite the differences in the concentration of Fe, similar

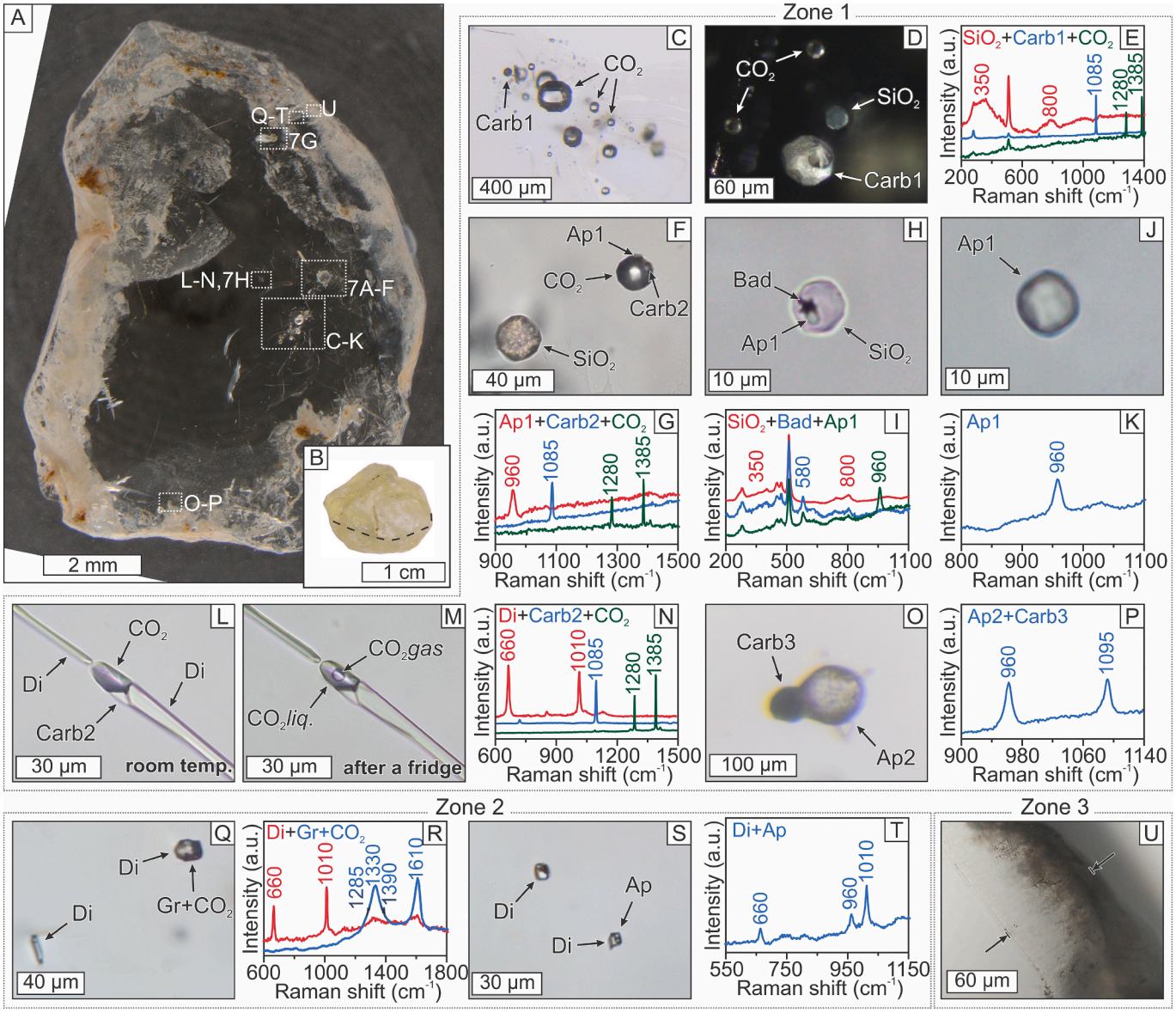

Fig. 3. The studied crystal of Itrongay feldspar and inclusions within it. A: transmitted light image of the mounted half of the crystal. White rectangles indicate the location of inclusions that are shown in Figs. 3C-U, 7A-H. B: the uncut crystal prior to mounting. Dashed line shows where the crystal was cut into halves and the slice for $^{40}Ar/^{39}Ar$ dating was obtained. C-U: optical microscope images of different types of inclusions and their Raman spectra. The same carbonate inclusion is visible in Fig. 3C and D, and the same SiO_2 and CO_2 inclusions are visible in Fig. 3D and F. Fig. 3L and M were taken before and after placing the mount into a fridge. Carb1, Carb2 and Carb3 are three types of carbonate. Ap1 and Ap2 are two types of apatite in zone 1, while Ap is apatite in zone 2. Di: diopside. Gr: graphite. See text for details.

BSE signal intensities were obtained from zones 1 and 2. Lower BSE signal intensities were obtained from subzone 3a, despite the fact that it has a lower Na/K ratio than zones 1 and 2. This indicates that the variations of the BSE signal intensities across (sub)zones 1, 2 and 3a largely characterise the orientation or the defectiveness of the crystal structure rather than variations in the mean atomic number (Lloyd, 1987; Robinson, 1980).

We have obtained eight in situ $^{40}Ar/^{39}Ar$ date profiles from the studied crystal, which are shown in Fig. 5A to H and are referred to as profiles A to H throughout. Arrows in Fig. 5I show the location of the profiles. Profile A traverses zone 1 and starts in the place where zone 1 is exposed at the original surface of the crystal and zones 2 and 3 are discontinuous and very thin, so that they could only contribute to the first one or two spot analyses. This profile starts with a date of ~420 Ma, which then gradually increases to ~455 Ma over the first ~500 μm and remains at this value across the subsequent ~1600 μm. Profile B was obtained from the central part of the crystal within zone 1 and only includes dates of ~455 Ma. Profiles C to F cross all three major zones, and each starts with a date of ~200 Ma, which corresponds to subzone 3a. The dates abruptly increase to ~385 Ma traversing towards the core of the crystal, which corresponds to subzone 2b, and then the dates gradually increase to ~405 Ma in profiles E and F, which corresponds to subzone 2a. Finally, an abrupt change to ~455 Ma occurs within zone 1 in all four profiles. Profile G only crosses subzones 3a and 2b and reproduces the corresponding part of the trend described for profiles C to F. Profile H only intersects subzone 2a and only includes dates of ~405 Ma. Overall, the obtained dates group into four clusters that correspond to (sub)zones 1, 2a, 2b and 3a, which can be easily recognised when they are plotted in descending order or used to plot histograms and probability density functions (Fig. 6A and B).

The $^{40}Ar/^{39}Ar$ dates obtained from any given (sub)zone are significantly scattered, giving rise to high MSWD values for their weighted

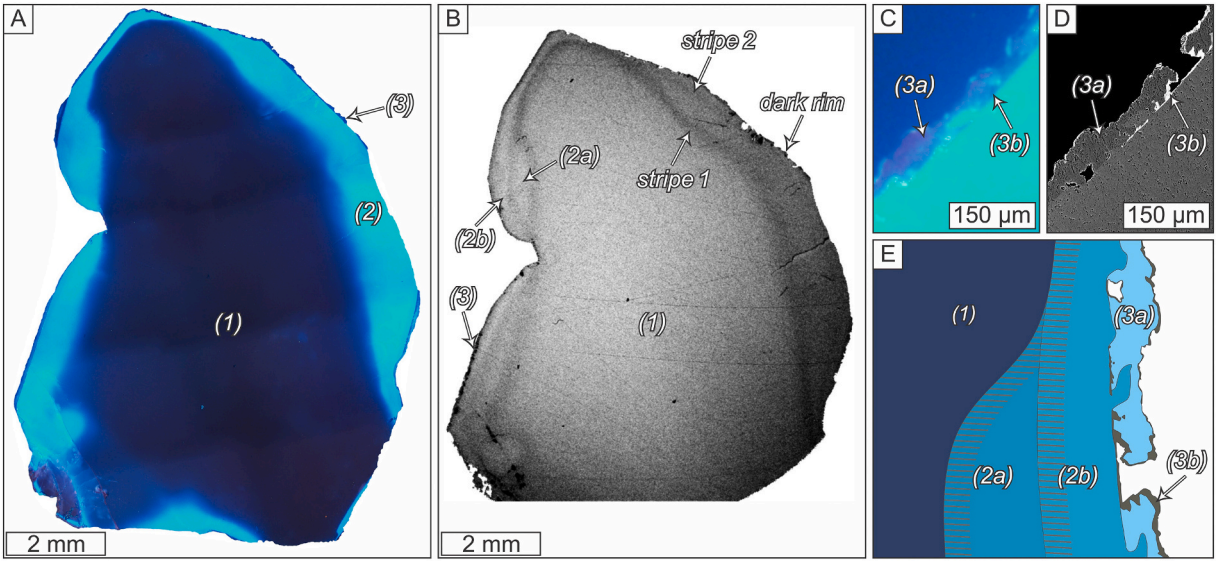

Fig. 4. BSE and CL images of the studied crystal of Itrongay feldspar. A: composite optical CL image of the entire crystal slice. Note the presence of three distinct zones: (1) a deep blue core, (2) a light blue intermediate zone and (3) a deep blue rim. B: BSE image of the entire crystal. This image was acquired for 16 min using a very high contrast setting, so that the observed differences in BSE signal intensity are not necessarily related to variations in composition. Note the presence of two dark stripes in the outer ~1 mm and a very dark outer rim. The most internal and more prominent stripe correlates with the beginning of zone 2 in Fig. 4A, while the second less prominent stripe splits zone 2 into two regions, which are designated 2a, from the beginning of the first stripe to the beginning of the second stripe, and 2b, from the beginning of the second stripe (or the first stripe where only one stripe is present) to the beginning of the very dark outer rim (zone 3). C-D: CL (C) and BSE (D) images of the outer ~300 µm of the crystal. The BSE image shows that zone 3 consists of two layers, which include a thicker and darker discontinuous layer adjacent to zone 2 (subzone 3a), and a thinner and brighter layer in the outermost part of the crystal (subzone 3b). E: schematic sketch (not to scale) showing the relationships between all the zones and subzones. Zone 1 corresponds to the core of the crystal with very weak CL. Zone 2 is the intermediate zone with light blue CL, and is divided into subzone 2a, which starts with the first dark stripe visible in the BSE image (shown with grey hatching), and subzone 2b, which starts with the second dark stripe visible in the BSE image (also shown with grey hatching). Zone 3 is the outer rim with very weak CL, which includes subzones 3a and 3b, corresponding to the dark and bright layers visible in the BSE images, respectively. For interpretation of the references to colour in this figure legend, the reader is referred to the web version of this article.

means (Fig. 6B). For example, with the exception of one date of ~434 Ma, all of the dates from zone 1 fall within the range of 440–466 Ma (average internal 2σ uncertainty is 5 Ma) with an MSWD value of 7.6 for their weighted mean (Fig. 6B). A comparable scatter within zone 1 is observed for the individual profiles. For example, all of the dates in profile B (zone 1 only) fall within the range of 447–463 Ma (average internal 2σ uncertainty is 6 Ma) with an MSWD of 2.9 for their weighted mean (Fig. 5B). These variations are unlikely to be related to analytical issues because in some cases the observed date variations along the profile have been reproduced by repeated measurements in the same area (Fig. 5B). While in some places the dates from any given (sub)zone consistently increase with increasing distance from the rim (e.g. first 500 µm in profile A, Fig. 5A), this is not always the case. For example, profile B has three segments of ~300 µm length where the dates in zone 1 consistently decrease with increasing distance from the upper tip of the crystal, each terminating with an abrupt increase of the dates (Fig. 5A). Another example is provided by profile F, where traversing towards the core of the crystal the dates in zone 2 consistently increase in the outer ~350 µm and then decrease in the subsequent ~150 µm (Fig. 5F). Nevertheless, the youngest dates from any given (sub)zone consistently decrease when traversing from the core towards the rim of the crystal, which is evident from the comparison of the weighted means of the second to fourth youngest dates shown in Fig. 6C (the first youngest dates were chosen to be excluded from the calculation of the weighted means to minimise the potential influence of outliers).

4.3. Apatite characterisation and U–Pb dating

Three apatite inclusions from zone 1 of the studied crystal were prepared for in situ U–Pb dating. Small pieces of feldspar with apatite inclusions were cut out, mounted separately in epoxy resin and ground to expose the inclusions at the surface. The largest of these inclusions was characterised by CL imaging and trace element mapping (Fig. 7), while the smaller inclusions were characterised using only CL imaging (Fig. 7G, H). All three inclusions are isometric, rounded and appear slightly turbid from the outside while being mostly clear inside (e.g. Fig. 7A). All of them are co-trapped with sub-isometric pyroxene crystals, which they partly surround in some places (e.g. Fig. 7B). The largest inclusion contains an inclusion of an unidentified phase (Fig. 7B). A small carbonate crystal is attached to the medium-sized inclusion (Fig. 7G). These apatite inclusions appear orange in CL images (Fig. 7B, G, H), although the CL signal is very weak and is weaker at the core than at the boundaries, where carbonate with bright orange luminescence occurs (Fig. 7G). This suggests that the orange colour of the apatite inclusions in the CL images can be related to the presence of a sub-microscopic layer of carbonate at their boundaries. The CL image of the largest inclusion revealed some irregular bright features (marked as alteration in Fig. 7B), which appear as slightly turbid volumes beneath the polished surface in transmitted light. Their appearance in the CL image is probably related to scattering of CL signal that comes from the side. Trace element mapping showed that this inclusion has higher concentrations of U, Th, La, Y, and Zr in the core than at the rim (see Fig. 7C and D for the U and La maps; all of the maps can be found in the Supplementary Figures). In contrast, Pb, Fe, Mn, Sr and Ba are homogeneously distributed within the largest apatite inclusion (see Fig. 7E and F for the Pb and Mn maps), although a special note should be made about Pb. It appears that there is a slight decrease in Pb concentrations from the top left to the bottom right part of the Pb map, however it occurs in the direction of the laser beam movement and is probably an artefact. An analogous decrease is observed in the Ca signal intensity map (Supplementary Figures), suggesting that the efficiency of apatite ablation has slightly decreased in the same direction, which could create artefacts. The presence of high amounts of Pb in the inclusion

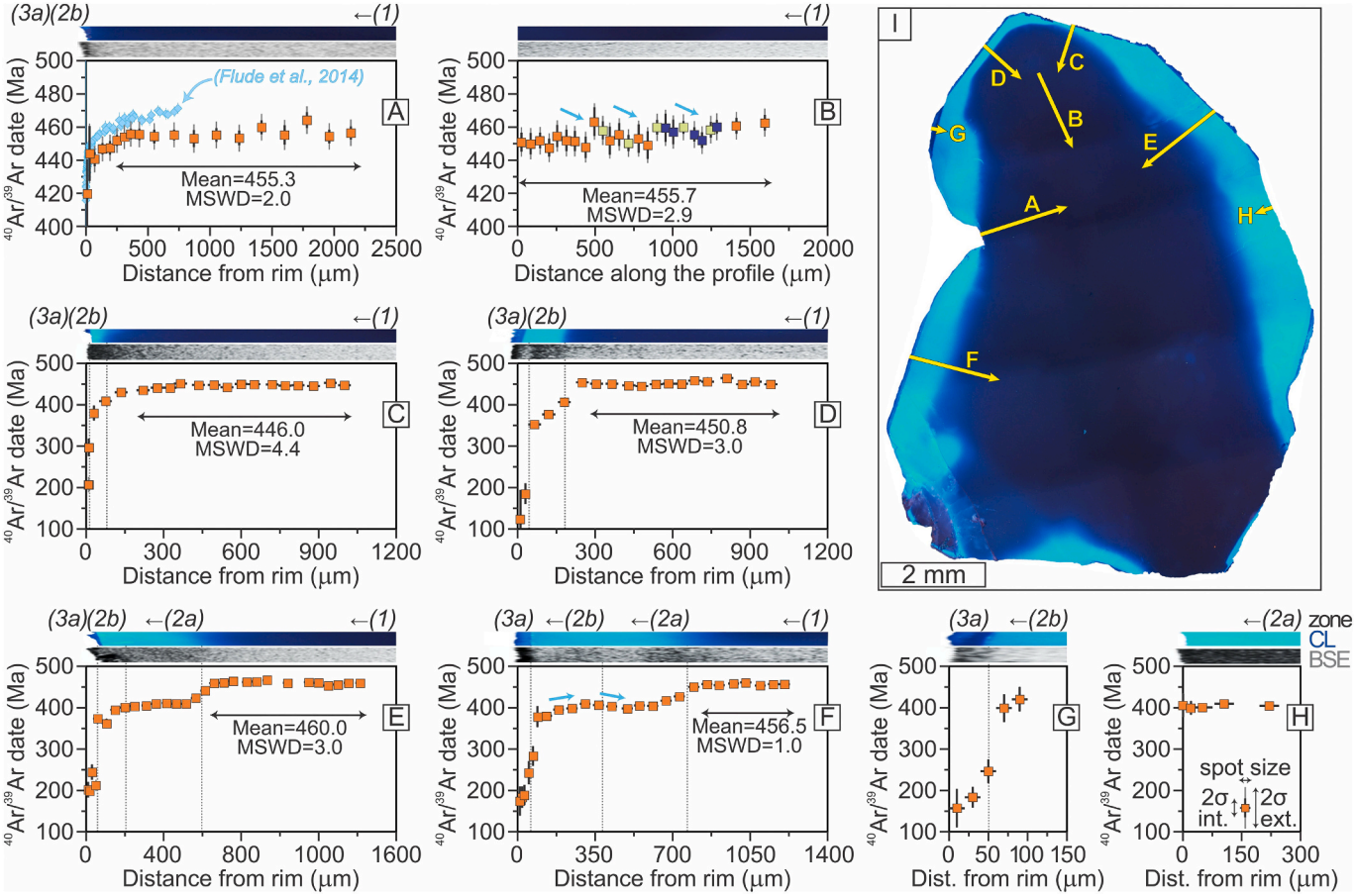

Fig. 5. In situ $^{40}Ar/^{39}Ar$ date profiles and their locations within the studied crystal of Itrongay feldspar. A-H: plots showing the variations of in situ $^{40}Ar/^{39}Ar$ dates along the profiles. Strip profiles above the date plots show the variations of BSE and CL signals. These were used to locate the boundaries between the zones, which are shown with grey dotted lines and are labelled above the plots. Blue markers in Fig. 5A show the composite in situ $^{40}Ar/^{39}Ar$ date profile from (Flude et al., 2014). Their dates were recalculated using the decay constants of (Steiger and Jäger, 1977), which changed these dates by < 0.1 Ma. Blue arrows in Fig. 5B and F indicate notable segments of the date profiles where the dates consistently increase or decrease with increasing distance from the rim of the crystal. The colour coded dates shown in Fig. 5B were obtained in a sequential order of light green, then orange, then deep blue, revealing their reproducibility. Weighted means and MSWD values shown in Fig. 5A-E were calculated for intervals that are indicated with double headed arrows, internal uncertainties were used in calculations. I: composite optical CL image with yellow arrows showing the location of the in situ $^{40}Ar/^{39}Ar$ date profiles. Arrowheads designate the righthand side of the plots in Fig. 5A-H. For interpretation of the references to colour in this figure legend, the reader is referred to the web version of this article.

within this apatite inclusion and at the apatite-feldspar boundary as in the bottom part of the Pb map could also affect our measurements. Therefore, we suggest that Pb is homogeneously distributed in this apatite inclusion. We observed no clear variations of trace element concentrations, including Pb, in feldspar around this inclusion (Supplementary Figures).

Three U–Pb dates were obtained from the largest apatite inclusion. A date of 569.2 ± 8.3 Ma was obtained from its U-rich core, while older and younger dates of 576.4 ± 8.5 Ma and 558.5 ± 8.5 Ma were obtained from its U-poor flanks (Fig. 7B, C, I). The location of the younger date is close to one of the irregular features that are visible in the CL image (Fig. 7B). Two overlapping U–Pb dates of 548.1 ± 7.7 Ma and 549.8 ± 7.9 Ma were obtained for the medium-sized inclusion (Fig. 7G, J). One U–Pb date of 530.0 ± 7.3 Ma was obtained from the smallest inclusion (Fig. 7H, K). There is an overall positive correlation between the U–Pb dates of these apatite inclusions and their half-widths (Fig. 7K).

5. Discussion

5.1. Genesis of Itrongay feldspar

Previous geochronological studies assumed that Itrongay feldspar formed in a single event at a relatively high temperature (> 500 °C; e.g. Nägler and Villa, 2000; Flude et al., 2014), which exceeds the expected temperature of its closure with respect to diffusive loss of ^{40}Ar (~440 °C, see Section 1). This assumption followed from two considerations. First, Itrongay feldspar is derived from a pegmatite, and pegmatites are considered to be products of melt crystallisation (e.g. Simmons and Webber, 2008). Second, Itrongay feldspar has a disordered orthoclase to low sanidine structure and a nm-scale tweed texture (Parsons and Lee, 2005; Wartho et al., 1999), which is typical of K-rich feldspars from intrusive rocks (e.g. Parsons et al., 2015). However, these considerations do not provide unequivocal evidence for crystallisation at high temperatures. Pegmatites are generally considered to crystallise from very undercooled melts and/or melts that are very rich in fluxing components such as B, F, P, Li and H_2O, and some estimates of their crystallisation temperatures (350–500 °C; Sirbescu and Nabelek, 2003a; Simmons and Webber, 2008; London et al., 2020) are close to the expected closure temperature of Itrongay feldspar. Furthermore, pegmatites frequently contain adularia (morphological variety of potassium feldspar; Černý and Chapman, 1984; Černý, 1994), which is typically formed in hydrothermal systems at ≲ 350 °C and is frequently characterised by high degrees of Si–Al disorder (Akizuki and Sunagawa, 1978; Černý and Chapman, 1986; Dong and Morrison, 1995; Rauchenstein-Martinek, 2014; Rossi and Rolland, 2014; Takahashi

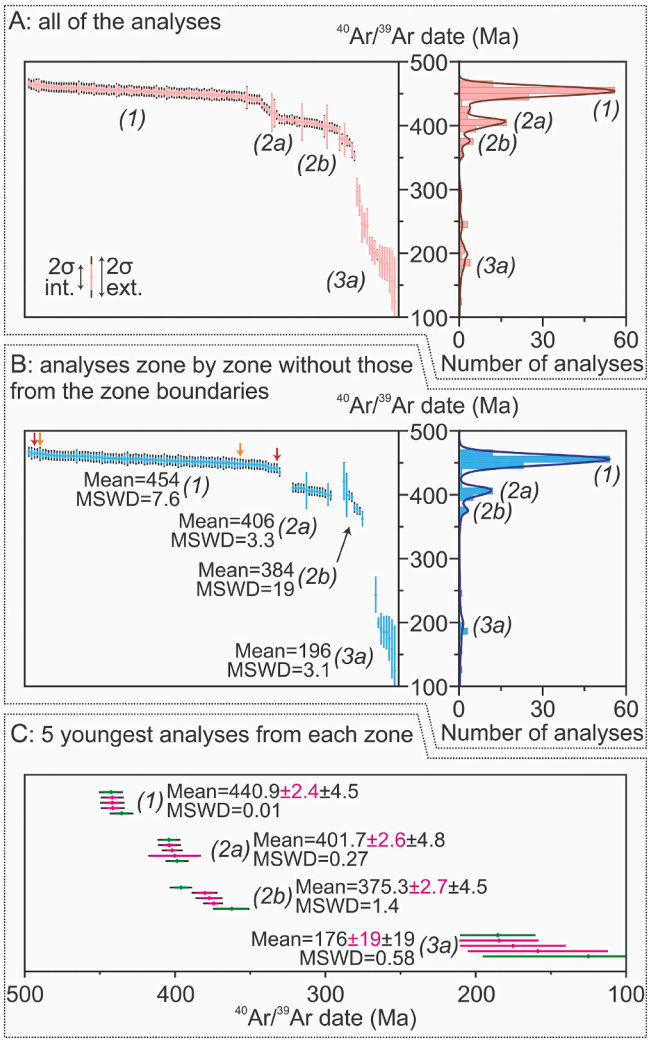

Fig. 6. A comparison of all of the in situ $^{40}Ar/^{39}Ar$ dates obtained in this work. A: all dates plotted in descending order along with a histogram and probability density function. B: dates from each (sub)zone plotted in descending order along with a histogram and probability density function. Weighted means were calculated for each of the (sub)zones. We have omitted dates that were obtained from the boundaries between the (sub)zones or proximal to these boundaries, as constrained using CL and BSE images, and these are also not included in the calculations of the weighted means. Brown and orange arrows show the youngest and the oldest dates in profiles A and B, respectively. C: the five youngest dates from each of the (sub)zones and weighted means calculated for the second to fourth youngest dates, internal uncertainties of which are shown in pink. All MSWD values were calculated using internal uncertainties. For interpretation of the references to colour in this figure legend, the reader is referred to the web version of this article.

et al., 2008). Notably, nm-scale cross-hatched twinning, which is referred to as a tweed texture, was first observed in adularia derived from an alpine cleft (McConnell, 1965).

Our field observations indicate that Itrongay feldspar, i.e. yellow gem-quality feldspar, is a minor constituent of the Itrongay pegmatite, which is predominantly composed of variably altered green feldspar and, in some places, smoky quartz. While the dominant variety of green feldspar becomes more yellow in some brecciated samples with smoky quartz, it still preserves a green hue. The only crystal of purely yellow feldspar that we found within a rock is hosted by brecciated and altered feldspar-dominated pegmatitic rock that was sampled near the contact with the host rocks of the Itrongay pegmatite. This suggests that the occurrence of Itrongay feldspar is not restricted to the quartz core of the Itrongay pegmatite. At the same time, purely yellow feldspar sometimes forms crystals with well-faceted tips, indicating that it grew into free spaces from some substrate. Therefore, Itrongay feldspar is likely a late phase that postdates the main sequence of pegmatite crystallisation. This is reminiscent of adularia reported from other pegmatites (Černý, 1994; Černý and Chapman, 1984), where it occurs in late veins and fills cavities that formed by leaching after the development of all pegmatite zones. Our petrographic observations indicate that the formation of Itrongay feldspar was sometimes a multi-stage process. The crystal that was chosen for this study formed by five discrete growth episodes, corresponding to (sub)zones 1, 2a, 2b, 3a and 3b. Irregular, wavy boundaries between the (sub)zones indicate that these growth episodes alternated with dissolution episodes (this texture is analogous to resorption zones in plagioclase from magmatic systems; Pearce and Kolisnik, 1990; Shcherbakov et al., 2011; Tsuchiyama, 1985).

Zones 1 and 2 are optically continuous and gem-quality. Zone 1 has a very weak CL response, which is unusual for magmatic feldspars (Görz et al., 1970; Götze et al., 2000; Smith and Stenstrom, 1965), but is typical for authigenic feldspars (Götze et al., 2000; Kastner and Siever, 1979; Krainer and Spötl, 1989; Lee and Parsons, 2003) and has been observed in adularia (Takahashi et al., 2008). In contrast, zone 2 has bright blue CL response, which is common in magmatic feldspars (Görz et al., 1970; Götze et al., 2000; Smith and Stenstrom, 1965). Zone 1 contains inclusions of liquid CO_2 and amorphous SiO_2. These have large sizes, well-developed negative crystal shapes and in one instance form a three-dimensional group, which indicates that they are primary inclusions of two co-existing substances from which zone 1 grew (Roedder, 1984). Amorphous SiO_2 inclusions yield Raman spectra that are typical of opal-CT (as opposed to silicate glass) and do not have shrinkage/fluid bubbles and daughter minerals, which are typically present in melt inclusions from pegmatites (Thomas et al., 2000, 2009; Thomas and Davidson, 2012a). They resemble some of "gel-like" inclusions that were reported from pegmatites (Fig. 11 in Thomas and Davidson, 2012b) and from chalcedony veins and amygdales in volcanic rocks (Fig. 3.1 in Khakimov, 1968). Liquid CO_2 is occasionally co-trapped with variably-sized carbonate, apatite and pyroxene crystals, while amorphous SiO_2 was co-trapped with apatite and baddeleyite crystals, suggesting that all these phases form an equilibrium assemblage with their host feldspar. Zone 2 has a different assemblage of inclusions, which comprises CO_2, graphite, pyroxene, apatite and an unidentified luminescent phase. The mineral inclusions are very small and frequently occur as polyphase intergrowths with rounded shapes, suggesting that they could be in disequilibrium with their host feldspar and potentially represent xenocrysts. The difference in the inventory of CL activators and the inclusion assemblage between zones 1 and 2 indicates that the physicochemical conditions of their crystallisation were not the same. However, the inclusion assemblages are not contrasting, and therefore these conditions could be broadly similar.

We are not aware of any other reports of an equilibrium assemblage that includes liquid CO_2, amorphous SiO_2, pyroxene, carbonate, apatite and baddeleyite. To our knowledge, only secondary CO_2 inclusions have been documented from pegmatites (Sirbescu and Nabelek, 2003b). CO_2 inclusions of variable density are common in granulite-facies metamorphic rocks, where they are interpreted to be trapped either at peak metamorphic conditions (e.g. Tsunogae et al., 2002; Touret and Huizenga, 2011) or during retrogression (Lamb et al., 1991, 1987). We could not find any reports of proven amorphous SiO_2 (not glass) inclusions in natural samples, although several studies have documented visually similar inclusions that were interpreted as inclusions of SiO_2-rich colloid solutions. The most visually similar inclusions have been described within cleavelandite from the Naipa pegmatite (Mozambique; Thomas and Davidson, 2012b) and within chalcedony from Cretaceous volcanic rocks near Ijevan (Armenia; Khakimov, 1968). Less similar inclusions that consist of quartz ± cristobalite ± FeOOH flakes in liquid ± gas have been reported from quartz and plagioclase from the Rønne pegmatite (Denmark; Thomas and Davidson, 2012b) and from achroite from the Malkhan pegmatite field (Russia; Thomas and

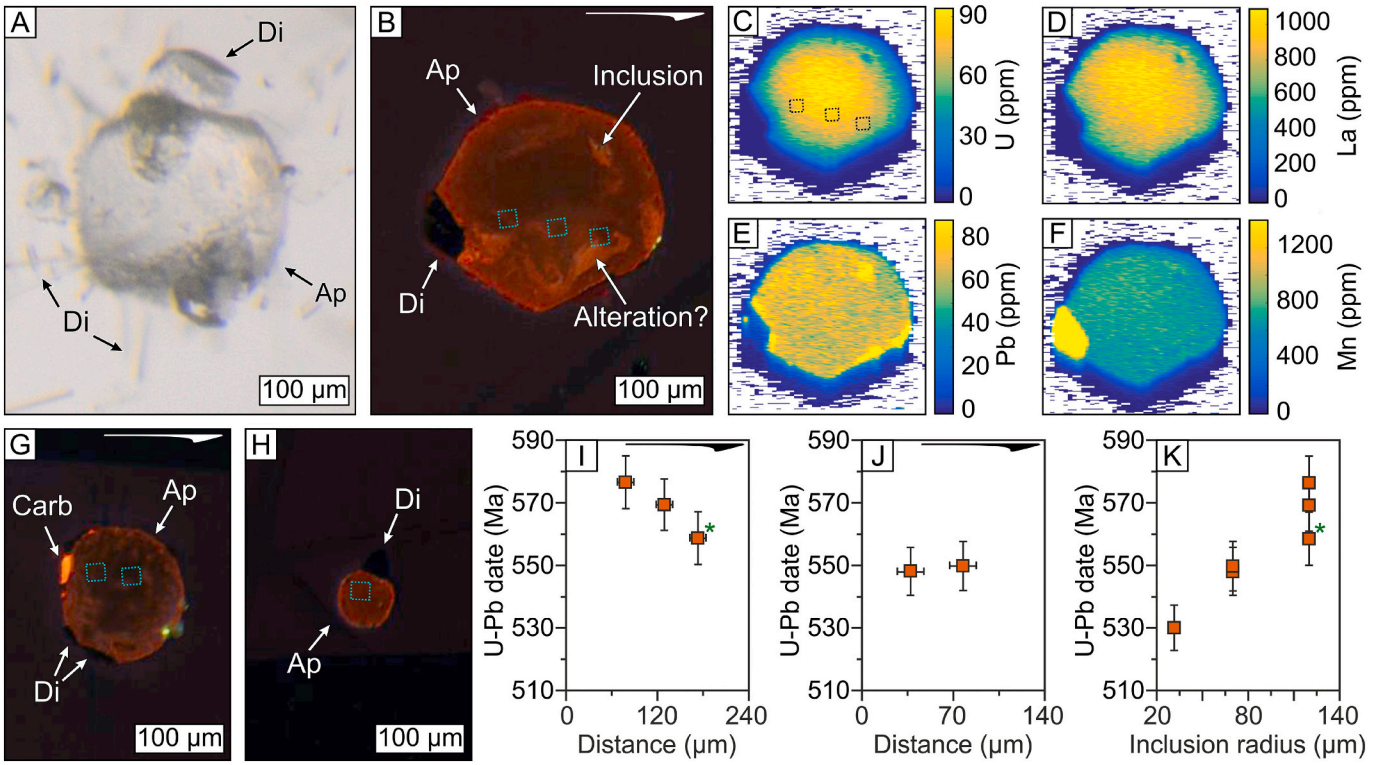

Fig. 7. Apatite inclusions from the studied crystal of Itrongay feldspar and their in situ U−Pb dates. Internal position of the inclusions is indicated in Fig. 3A. A-F: transmitted light (A) and CL (B) images and representative trace element maps (C−F) of the largest inclusion. G-H: CL images of the medium-sized (G) and smallest (H) inclusions. I-J: rim-core-rim variations of U−Pb dates in the largest (I) and medium-sized (J) inclusions. K: the relationship between the radii of the inclusions and their U−Pb dates. Square outlines in Figs. 7B-C, G-H indicate the analysis positions. Arrows in Fig. 7B and G designate the righthand side of the plots in Fig. 7I and J, respectively. Green asterisks in Fig. 7I, K indicate date that was presumably affected by alteration (see Section 5.2). Ap: apatite. Di: diopside. Carb: carbonate. For interpretation of the references to colour in this figure legend, the reader is referred to the web version of this article.

Davidson, 2008). Synthetic inclusions of SiO_2-rich liquids have been obtained in K_2O-CO_2-SiO_2-H_2O (Wilkinson et al., 1996) and Na_2O-CO_2-SiO_2-(Al_2O_3)-H_2O (Kotel'nikova and Kotel'nikov, 2011) systems and some other systems containing F and B (e.g. Peretyazhko et al., 2010 and therein). The presence of colloidal SiO_2 has been advocated for some hydrothermal systems that crystallise adularia (Dong and Morrison, 1995; Saunders, 1994; Takahashi et al., 2008).

While we do not have precise thermometric data for the CO_2 inclusions, our observations combined with those of Touret (1977) suggest that their homogenisation temperature is very close to room temperature and thus likely lies in the range of 15–25 °C. Isochores calculated for feldspar-hosted CO_2 inclusions with homogenisation temperatures of 15–25 °C using the FLUIDS software (Bakker, 2003; equations of state after Duan et al., 1992, 1996) do not cross the pressure-temperature fields experienced by the rocks of the Androyan domain during peak metamorphism and retrogression (Fig. 8; Markl et al., 2000; Tucker et al., 2014). Hence, we conclude that the Itrongay feldspar formed after the metamorphic events that are recorded in the rocks of southern Madagascar. Notably, post-metamorphic circulation of CO_2-dominated fluids has been proposed for other granulite-facies terranes (Lamb et al., 1991, 1987). The isochores cross the pressure-temperature fields where SiO_2-rich liquids have been experimentally synthetized by Wilkinson et al. (1996) and Kotel'nikova and Kotel'nikov (2011) (Fig. 8). Therefore, it is reasonable to assume that Itrongay feldspar formed in a similar system comprising dense SiO_2-rich colloid solution and CO_2-dominated fluid. Considering that the proposed crystallisation ages of zones 1 and 2 differ by ≳75 Ma (see Section 5.3), and zone 1 contains xenocrysts of apatite (see Section 5.2), it is also reasonable to assume that CO_2-dominated fluid was derived from the surrounding metamorphic rocks rather than representing the residual of pegmatite melt crystallisation.

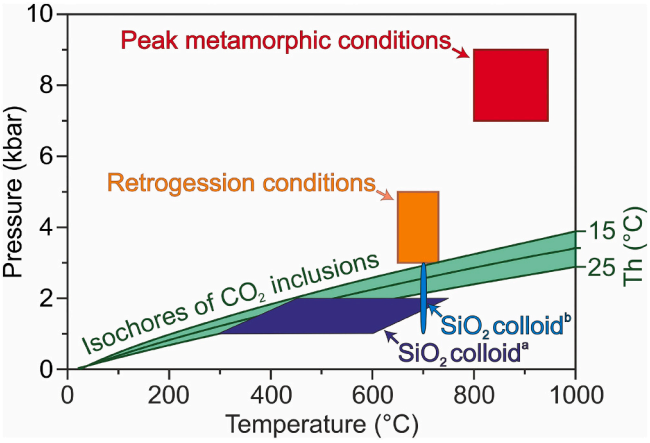

Fig. 8. A comparison of the crystallisation pressure and temperature estimates for Itrongay feldspar and for the surrounding metamorphic rocks of the Androyan domain. The pressure-temperature field of Itrongay feldspar crystallisation that satisfies isochores of CO_2 inclusions is shown in green. Dark green isochores were calculated using FLUIDS (Bakker, 2003; equations of state after Duan et al., 1992, 1996) assuming homogenisation temperatures 15, 20 and 25 °C. Red and the orange rectangles depict the pressure-temperature conditions that were attained within the Androyan domain during peak metamorphism and retrogression, respectively (Markl et al., 2000; Tucker et al., 2014). Blue fields show the pressure-temperature conditions where SiO_2-rich liquids were obtained in the experiments of (a) Wilkinson et al. (1996) and (b) Kotel'nikova and Kotel'nikov (2011). For interpretation of the references to colour in this figure legend, the reader is referred to the web version of this article.

Zone 3 is different from zones 1 and 2 because it has a very weak CL response, which is typical of authigenic feldspar (Götze et al., 2000; Kastner and Siever, 1979; Krainer and Spötl, 1989), and is also optically similar to authigenic feldspar (Lee and Parsons, 2003; Worden and Rushton, 1992). The optical similarities include (i) a turbid appearance due to the presence of very small inclusions, (ii) simultaneous extinction across the zone in cross-polarised light, rendering it optically continuous, and (iii) asynchronous extinction with zones 1 and 2 in cross-polarised light, revealing an optical discontinuity with the rest of the crystal. Therefore, we suggest that zone 3 is analogous to authigenic felspar from sedimentary rocks and thus likely formed from H_2O-rich fluid (Kastner and Siever, 1979).

Unfortunately, quantitative estimates of the temperature at which any given zone of the studied crystal formed cannot be made with the available data. However, several lines of evidence suggest that Itrongay felspar could have formed and subsequently remained at lower temperatures than previously assumed. First, zones 1 and 3 have very weak luminescence, which has only been observed in authigenic feldspar and hydrothermal adularia that were estimated to have formed at temperatures below ~300 °C (Kastner and Siever, 1979; Lee and Parsons, 2003; Takahashi et al., 2008). Second, the estimated temperatures of adularia crystallisation in hydrothermal systems that were suggested to have had colloidal SiO_2 fall within the range of 150–285 °C (Dong and Morrison, 1995; Takahashi et al., 2008). Third, in sedimentary rocks opal-CT transforms to quartz at > 100 °C, albeit in the presence of H_2O-rich fluid (Behl, 2011; Keller and Isaacs, 1985). Therefore, it is conceivable that each subzone in the studied crystal rapidly crystallised at ≲300 °C and subsequently cooled to < 100 °C. While there are no experimental data that can be directly compared with our observations, data for apparently similar systems suggest that SiO_2-rich liquids can form at temperatures as low as ~300 °C (Wilkinson et al., 1996) and remain liquid even at ~250 °C (Kotel'nikova and Kotel'nikov, 2011). Further petrological and/or experimental studies are required to estimate precisely the temperature (and pressure) of Itrongay feldspar crystallisation.

5.2. Apatite inclusions and their U–Pb dates

We have characterised and dated three apatite inclusions from zone 1 of the studied Itrongay feldspar crystal. These inclusions were isometric, rounded and appeared slightly turbid when viewing from the side due to surface roughness, which is probably related to natural etching before their entrapment. Trace element mapping of the largest inclusion revealed concentric zoning in U, Th, La, Y, and Zr, indicating that trace elements were evenly supplied from every side during its crystallisation. All of these characteristics suggest the apatite inclusions formed before being trapped within the feldspar, and thus they are protogenetic inclusions. The U–Pb dates of these inclusions (530.0 ± 7.3 to 576.4 ± 8.5 Ma) exceed the $^{40}Ar/^{39}Ar$ dates of their host feldspar (120 ± 70 Ma to 466 ± 8 Ma) by > 50–100 Ma (Fig. 9). They also exceed by the same amount all of the previous $^{40}Ar/^{39}Ar$ dates (416 ± 3 Ma to 474 ± 5 Ma; Arnaud and Kelley, 1997; Flude et al., 2014; Nägler and Villa, 2000) and the previous K–Ca date (477 ± 2 Ma; Nägler and Villa, 2000) of Itrongay feldspar (Fig. 9). While the difference between the U–Pb dates and the $^{40}Ar/^{39}Ar$ dates can in principle be explained by assuming that the apatite inclusions and their host feldspar are of the same age and that the host feldspar has partially lost ^{40}Ar by diffusion, such explanation would contradict the observation that the U–Pb dates are much older than the K–Ca date of Itrongay feldspar, albeit not of the same crystal. If this assumption was accurate, the K–Ca date would be expected to exceed the U–Pb dates, since Ca diffusion in potassium feldspar (Cherniak and Watson, 2019) is slower than Pb diffusion both in potassium feldspar (Cherniak, 2010b) and apatite (Cherniak, 2010a). Another contradiction to this assumption is that there is no elevated $^{206,207}Pb$ concentrations in the feldspar adjacent to these inclusions, which would be expected considering that Pb diffusion in potassium feldspar (Cherniak, 2010b) is slower than in apatite (Cherniak, 2010a). Therefore, we suggest that the dated apatite inclusions are older than their host feldspar and represent xenocrysts. Considering that each of these apatite xenocrysts is contiguous with a pyroxene crystal, it seems reasonable to assume that they were derived from one of the pyroxene-bearing rocks that host the Itrongay pegmatite.

Different inclusions yielded different U–Pb dates (Fig. 7K). These variations could be explained by suggesting that the dated inclusions were derived from different rocks. However, considering the following two observations, it seems more likely that these inclusions were derived from the same rock. First, the mineralogical diversity of inclusions in zones 1 and 2 in the studied feldspar crystal is relatively narrow, while the assemblages of potential xenocrysts are different. For example, graphite is only present in zone 2. This suggests that the fluids from which any given zone grew carry xenocrysts from a limited amount of sources rather than from every rock in southern Madagascar (note that graphite is relatively common in them, e.g. de Wit et al., 2001). Second, all three dated inclusions have similar appearance in CL images and each of them is contiguous with a pyroxene crystal. This suggests that they could have been part of the same rock. If the dated inclusions are from the same rock, then what accounts for the variation in their U–Pb dates? Considering that they were carried and apparently even etched by fluids, the first guess would probably be the fluid-induced recrystallisation. The CL image of the largest inclusion has some irregular bright features that appear as slightly turbid volumes beneath the polished surface in transmitted light. By analogy with alkali feldspar, where turbidity usually develops by fluid-induced recrystallisation (e.g. Parsons et al., 2015; Parsons and Lee, 2005), we suggest that these turbid volumes represent altered apatite. However, this visible alteration has affected relatively small volumes within the inclusion and probably occurred simultaneously with the above-mentioned natural etching (there is no evidence of alteration in surrounding feldspar). Only in one of our U–Pb analyses we sampled from such altered volume (not intentionally), which gave the youngest U–Pb date from the largest inclusion (marked with asterisk in Fig. 7I). Other U–Pb analyses were obtained from pristine volumes, and there is no evidence to suggest that these volumes were affected by alteration (such as different U/Th ratios in trace element maps). Therefore, we suggest that fluid-induced recrystallisation did not play a significant role in resetting U–Pb dates of these apatite inclusions. The remaining alternative is that the observed U–Pb date variations result from the diffusive loss of $^{206,207}Pb$ that occurred before the dated xenocrysts were entrained by the fluid from which their host feldspar grew. It may seem at a first glance that such interpretation is contradicted by the fact that Pb is homogeneously distributed in the largest inclusion (Fig. 7E) rather than showing a decrease in concentration towards the rim. However, two things need to be pointed out here. First, following previous application of apatite U–Pb thermochronometer (Chamberlain and Bowring, 2001; Cochrane et al., 2014; Paul et al., 2019, 2018; Schoene and Bowring, 2007), only radiogenic $^{206,207}Pb$ is expected to show bell-shaped rim-core-rim concentration gradients, not total. Second, the very expectation of such gradients is based on the assumption that radiogenic $^{206,207}Pb$ is lost to an infinite reservoir as soon as it reaches the boundary of apatite crystal, which has not been systematically tested, and violation of which can result in homogeneously distributed $^{206,207}Pb$ in apatite (both total and radiogenic; Popov and Spikings, 2018). The only prediction of the diffusive loss of radiogenic $^{206,207}Pb$ that can be checked using our data is the presence of positive correlation between the U–Pb dates of the inclusions and their sizes (e.g. Dodson, 1973; Cochrane et al., 2014; Popov and Spikings, 2018), and there is such correlation (Fig. 7K). In the absence of significant alteration this correlation indicates that the obtained U–Pb dates likely were partially reset by diffusion.

While the dated apatite inclusions seem to have lost $^{206,207}Pb$ by diffusion, their xenocrystic origin and natural etching render them

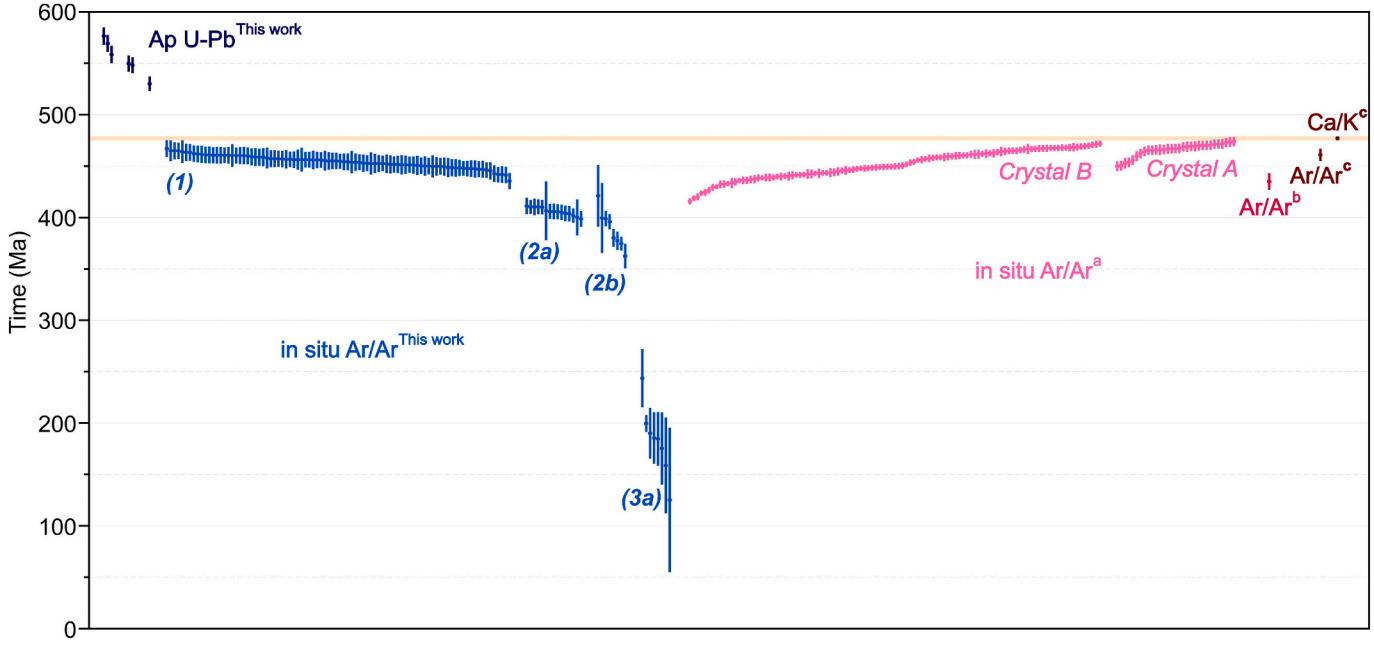

Fig. 9. A comparison of the available geochronological data for the Itrongay pegmatite. Isotopic dates from our work are compared with (a) in situ $^{40}Ar/^{39}Ar$ dates from Flude et al. (2014), (b) $^{40}Ar/^{39}Ar$ plateau date from Arnaud and Kelley (1997), (c) $^{40}Ar/^{39}Ar$ plateau date and K–Ca isochron date from Nägler and Villa (2000). Our $^{40}Ar/^{39}Ar$ dates are grouped by (sub)zones and $^{40}Ar/^{39}Ar$ dates that were obtained from the boundaries between the (sub)zones are not shown. 2σ external uncertainties are shown in all cases except for crystal B from Flude et al. (2014), where the nature of 2σ uncertainty is unclear to us (not specified in the original work, potentially internal). Horizontal line of pale orange colour shows the K–Ca date from Nägler and Villa (2000) with 2σ external uncertainty.

poorly suited for thermochronology. The size of the dated inclusions was apparently reduced to an unknown extent by etching, it is impossible to constrain how boundary conditions changed through time, and there still is a chance that these inclusions were derived from three different rocks with similar lithology but different histories. Any time-temperature path derived by inversion modelling of our U–Pb data would be of questionable reliability. The only point of such modelling would be to show that a time-temperature solution can be found, and that this solution is not completely unreasonable when compared with a priori knowledge of regional geology. A failure to show this would falsify our hypothesis that the dated apatite inclusions were derived from the same rock. Even without inversion modelling our results indicate that at the time when Itrongay feldspar formed, some rock adjacent to the Itrongay pegmatite contained apatite that apparently lost $^{206,207}Pb$ by diffusion. This rock would be a perfect target for any further attempt to constrain the thermal history of the host rocks of the Itrongay pegmatite using fully appropriate material. It is also important to note that some apatite inclusions in the studied crystal of Itrongay feldspar appear to be cogenetic with it. We were unable to successfully find and prepare for analysis sufficiently large inclusions of this kind, but it might be possible to find them in some other crystal of Itrongay feldspar.

5.3. $^{40}Ar/^{39}Ar$ dates of Itrongay feldspar

We obtained eight in situ $^{40}Ar/^{39}Ar$ date profiles traversing (sub) zones 1, 2a, 2b and 3a of the studied Itrongay feldspar crystal. The $^{40}Ar/^{39}Ar$ dates range from 120 ± 70 Ma to 466 ± 8 Ma (2σ ext.), and overlap with previously reported $^{40}Ar/^{39}Ar$ dates of Itrongay feldspar, including plateau dates of 435 ± 8 Ma (Arnaud and Kelley, 1997) and 461 ± 6 Ma (Nägler and Villa, 2000) and in situ dates ranging from 416 ± 3 Ma to 474 ± 5 Ma (Flude et al., 2014; Fig. 9). Most of the $^{40}Ar/^{39}Ar$ dates are younger than the K–Ca isochron date of 477 ± 2 Ma that was obtained for Itrongay feldspar (Nägler and Villa, 2000; Fig. 9). Previous studies suggested that the intra-grain variation of the $^{40}Ar/^{39}Ar$ dates (Flude et al., 2014) and the differences between the $^{40}Ar/^{39}Ar$ dates and the K–Ca date (Flude et al., 2014; Nägler and Villa, 2000) solely result from the diffusive loss of ^{40}Ar. It was also argued that Itrongay feldspar crystals acted as grain-scale diffusion domains during their geologic histories (Flude et al., 2014). However, as we discuss below, our results are not consistent with these interpretations, as well as any other previously proposed model for the diffusive loss of ^{40}Ar.

An excess of the K–Ca date reported by Nägler and Villa (2000) over the $^{40}Ar/^{39}Ar$ date of the same sample (Nägler and Villa, 2000) and the majority of $^{40}Ar/^{39}Ar$ dates of other samples (this work; Arnaud and Kelley, 1997; Flude et al., 2014) indicates that Itrongay feldspar may have partially lost ^{40}Ar by diffusion. However, two of our observations are incompatible with the diffusive loss of ^{40}Ar via a single mechanism from a grain-scale diffusion domain with homogeneously distributed ^{40}K (i.e. following the proposition of Flude et al., 2014), which is expected to produce smooth bell-shaped rim-core-rim $^{40}Ar/^{39}Ar$ date profiles with monotonically decreasing $^{40}Ar/^{39}Ar$ dates towards the crystal rims. First, many of the $^{40}Ar/^{39}Ar$ date profiles obtained here have a staircase topology (Fig. 5D-G). Second, while the obtained $^{40}Ar/^{39}Ar$ dates generally decrease with increasing distance from the crystal core, some deviations from this trend occur. Profile B shows that in some regions within zone 1 the $^{40}Ar/^{39}Ar$ dates steadily increase over a distance of ~300 μm when approaching the crystal rim, after which they abruptly decrease (Fig. 5B). Profile F shows an analogous relationship within zone 2 (Fig. 5F). The first observation can in principle be accounted for by invoking multi-path diffusion (e.g. Lee, 1995; Baxter, 2010) or diffusion via several mechanisms (by analogy with Li in olivine in Dohmen et al., 2010) from a grain-scale diffusion domain with homogeneously distributed ^{40}K. However, both these scenarios are expected to produce $^{40}Ar/^{39}Ar$ dates that steadily decrease when approaching the crystal rim, which conflicts with the second observation. This complication can in principle be accounted for by introducing unevenly distributed traps for ^{40}Ar, and as we discuss in the next paragraph there are potential candidates for this role. However, the resulting model would probably be excessively ad hoc, and there is no evidence to support any hypothetical distribution of short

circuits or the use of several diffusion mechanism. Finally, when combined with the results of Ar diffusion experiments on Itrongay feldspar (Arnaud and Kelley, 1997; Cassata and Renne, 2013; Wartho et al., 1999), our second observation is inconsistent with the diffusive loss of ^{40}Ar that would be compatible with multi-diffusion domain theory of Lovera et al. (1989). Abrupt changes in the ^{40}Ar/^{39}Ar dates along the profiles imply that the size of any intra-grain diffusion domain cannot significantly exceed the size of an ablation pit with 50 μm diameter, which is incompatible with the diffusion experiments, since they suggest that much larger Itrongay feldspar fragments generally behave as grain-scale diffusion domains during laboratory outgassing. Therefore, we suggest that while some diffusive loss of ^{40}Ar may have occurred, it does not represent the main factor accounting the observed variability in ^{40}Ar/^{39}Ar dates.

The most significant changes in dates along the ^{40}Ar/^{39}Ar date profiles obtained here correspond to the boundaries between different (sub)zones (Fig. 5A-H), and different (sub)zones yield distinguishable average ^{40}Ar/^{39}Ar dates that steadily decrease when approaching the crystal rim (Fig. 6B). This suggests that the major component in the observed ^{40}Ar/^{39}Ar date variations likely reflects the real crystallisation age differences between the described (sub)zones. However, several observations indicate that these variations cannot be entirely explained by the crystallisation age variations. First, in several places ^{40}Ar/^{39}Ar dates increase towards the rim, for example in zone 1 in profile B (5B) and in zone 2 in profile F (Fig. 5F). Second, any given (sub)zone yields significantly scattered ^{40}Ar/^{39}Ar dates, which is expressed in high MSWD values that are calculated for their weighted means (Figs. 5A-E, 6B). Third, a comparison of the ^{40}Ar/^{39}Ar dates obtained here and in Arnaud and Kelley (1997), Nägler and Villa (2000), and Flude et al. (2014) with the K–Ca date from Nägler and Villa (2000) indicates that some diffusive loss of ^{40}Ar may have occurred (Fig. 9). The available evidence is yet not sufficient to reliably identify the cause(s) of these complications. Probably, some component in the observed variability of in situ ^{40}Ar/^{39}Ar dates is related to the presence of nm-scale inclusions of an unidentified mineral, which were previously reported from Itrongay feldspar (Parsons and Lee, 2005; Wartho et al., 1999). We envisage two end-member models (A and B), both of which assume that the inclusions are unevenly distributed within Itrongay feldspar (as was suggested by the cited studies), and have low Cl and Ca concentrations (to account for the absence of Cl-derived ^{38}Ar and Ca-derived ^{37}Ar in our analyses). Model A further assumes that the inclusions host excess or inherited ^{40}Ar within them or excess ^{40}Ar at their boundaries, so that the regions with abundant inclusions yield older ^{40}Ar/^{39}Ar dates (Fig. 10). Model B further assumes that some radiogenic ^{40}Ar diffused into the boundaries of these inclusions during the geologic past and escaped from them during sample preparation, for example due to microcracking. In this case, regions with higher concentrations of inclusions would yield younger ^{40}Ar/^{39}Ar dates (Fig. 10). An analogous model was proposed in Arnaud and Kelley (1997), who conducted several step-heating and in vacuo crushing experiments with Itrongay feldspar. Their step-heating ^{40}Ar/^{39}Ar data suggested partial loss of ^{40}Ar from the outer 5–10 μm of the analysed fragments irrespective of where these fragments were located in the original crystal. Their in vacuo crushing experiments suggested that a considerable amount of ^{40}Ar is stored in relatively Cl-free traps (almost no Cl-derived ^{38}Ar was detected). Their preferred interpretation is that some of ^{40}Ar diffused into the traps during geologic past and escaped the analysed fragments when the traps were opened by sample preparation.

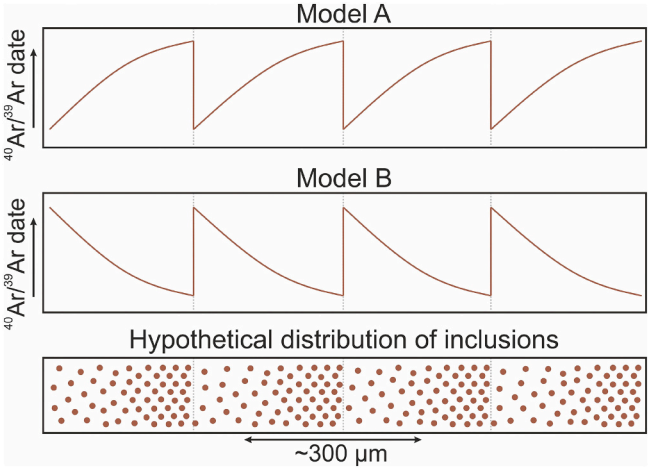

Fig. 10. Hypothetical relationships between the intra-grain ^{40}Ar/^{39}Ar date variation and the abundance of inclusions.

While further studies are clearly required to verify the proposed models, we speculate that both come into play in the studied crystal of Itrongay feldspar. Model A provides a reasonable explanation for fact that the oldest ^{40}Ar/^{39}Ar dates obtained from zone 2 in profile F were obtained from the boundary between subzones 2a and 2b. This boundary appears as a dark wavy stripe in the BSE image of the studied crystal, indicating that it may contain an increased amount of some crystal structure defects, potentially inclusions with excess or inherited ^{40}Ar (consider that zone 2 is optically continuous). However, model A cannot readily explain why all of the ^{40}Ar/^{39}Ar dates that were obtained here and previously (Arnaud and Kelley, 1997; Flude et al., 2014; Nägler and Villa, 2000) are younger than the K–Ca date of Itrongay feldspar (Nägler and Villa, 2000). Model B can account for the discrepancy between the ^{40}Ar/^{39}Ar and K–Ca dates by relating it to the diffusive loss of ^{40}Ar (followed by the loss of ^{40}Ar induced by sample preparation). However, it is not trivial to invoke model B as an explanation for relatively old ^{40}Ar/^{39}Ar dates from the boundary between subzones 2a and 2b, as it would require that the inclusions are less abundant at the boundary than around it and thus contradict the results of BSE imaging. Therefore, we suggest that the ^{40}Ar/^{39}Ar date variations in zone 1 are explained by model B, while the ^{40}Ar/^{39}Ar date variations in zones 2 and 3 are explained by model A. Following model B, the previously reported K–Ca date of 477 ± 2 Ma (Nägler and Villa, 2000) can be interpreted as the crystallisation age of zone 1, while the youngest ^{40}Ar/^{39}Ar dates obtained from this zone, which have a weighted mean of 440.9 ± 4.5 Ma, can be interpreted as the age of cooling through an unconstrained temperature. Following model A, the youngest ^{40}Ar/^{39}Ar dates that we obtained from subzones 2a, 2b and 3a, which have weighted means of 401.7 ± 4.8 Ma, 375.3 ± 4.5 Ma and 176 ± 19 Ma, respectively, are least affected by excess or inherited ^{40}Ar and thus can be interpreted as the crystallisation ages of these subzones. Notably, the composite ^{40}Ar/^{39}Ar date profile presented in Flude et al. (2014) is similar to our profile A (Fig. 5A). While we cannot rule out the possibility that the interpretation made in Flude et al. (2014) is accurate, this similarity suggests that it could have resulted from not recognising the presence of thin overgrowths of younger feldspar. Their crystal did not have noticeable overgrowths of turbid feldspar like ours, but it could have had overgrowths of gem-quality feldspar similar to zone 2 in the crystal studied here.

6. Summary and implications

Collectively our petrological and geochronological interpretations suggest that the studied Itrongay feldspar crystal formed during five discrete growth episodes that were separated from each other by tens to hundreds of millions of years. Each growth episode postdates high-temperature metamorphism that is recorded regionally across the Androyan domain. Zone 1 precipitated from co-existing CO_2-dominated fluid and dense SiO_2-rich colloid solution, and its crystallisation age is estimated to be 477 ± 2 Ma (K–Ca date reported by Nägler and Villa, 2000). The ^{40}Ar/^{39}Ar dates obtained from this zone are interpreted to

be partly reset by the diffusive loss of ^{40}Ar. Subzones 2a and 2b probably formed in a similar environment, and their crystallisation ages are estimated to be 401.7 ± 4.8 Ma and 375.3 ± 4.5 Ma, respectively (weighted means of the second to fourth youngest ^{40}Ar/^{39}Ar dates). Subzones 3a and 3b appear analogous to authigenic feldspar from sedimentary rocks and thus may have precipitated from H_2O-rich fluid. The crystallisation age of subzone 3a is estimated to be 176 ± 19 Ma (weighted mean of the second to fourth youngest ^{40}Ar/^{39}Ar dates), while subzone 3b is too thin to be dated. Some small apatite inclusions within zone 1 (the crystal core) are cogenetic with the host feldspar. However, the three large apatite inclusions that we used for U−Pb dating are xenocrysts that could have been derived from the pyroxene-bearing rocks that host the Itrongay pegmatite. The U−Pb dates of these xenocrysts are interpreted to be partially reset by the diffusive loss of radiogenic ^{206,207}Pb that occurred before trapping by the feldspar crystal.

Our results have important implications for ^{40}Ar/^{39}Ar dating of alkali feldspar and U−Pb dating of apatite. The ^{40}Ar/^{39}Ar data acquired here are inconsistent with the suggestion of Flude et al. (2014) that Itrongay feldspar partially lost ^{40}Ar by volume diffusion through a continuous crystal structure without any complications related to the presence of crystal structure defects. In combination with the results of previous diffusion experiments on Itrongay feldspar (Arnaud and Kelley, 1997; Cassata and Renne, 2013; Wartho et al., 1999), these data are also inconsistent with the model of the diffusive ^{40}Ar loss offered by multi-diffusion domain theory (Lovera et al., 1989). Furthermore, while the studied Itrongay feldspar crystal probably experienced some diffusive loss of ^{40}Ar (via yet unconfirmed model B; Section 5.3), much greater component in the observed ^{40}Ar/^{39}Ar date variations is the result of fluid-induced dissolution and overgrowth. Clearly, there is a lack of unambiguous evidence for the diffusive loss of ^{40}Ar from alkali feldspar that can be quantitatively interpreted using existing models, and further research is needed to develop a framework for reconstructing the thermal histories of rocks using this mineral. Our results also show that in situ ^{40}Ar/^{39}Ar dating of alkali feldspar combined with petrological characterisation is a promising tool for tracking fluid flow events in the Earth's crust, which can seek applications beyond authigenic K-rich feldspars from sedimentary rocks (e.g. Hagen et al., 2001; Mark et al., 2007) and perhaps used in a way analogous to U-Th-Pb dating of texturally different domains within gem-quality monazite from alpine clefts (e.g. Bergemann et al., 2017; Ricchi et al., 2019). Our apatite U−Pb data suggest that in some cases ^{206,207}Pb can be lost from apatite by volume diffusion without significant contribution from chemical alteration, supporting previous suggestions that U−Pb dating of apatite can be used for thermochronology (Chamberlain and Bowring, 2001; Cochrane et al., 2014; Paul et al., 2019, 2018; Schoene and Bowring, 2007).

The most important implication of our work for the geology of southern Madagascar is that it provides evidence for multiple episodes of fluid circulation which occurred after the Ediacaran to early Cambrian high-temperature metamorphism. This adds to several previous studies that invoked fluid-induced dissolution-reprecipitation to explain some U-(Th)-Pb dates of monazite (Fernandez et al., 2003; Grégoire et al., 2009; Martelat et al., 2000) and titanite (Holder and Hacker, 2019) and ^{40}Ar/^{39}Ar dates of micas (Fernandez et al., 2003) derived from Madagascan rocks. Collectively, these results show that resetting of isotopic dates by fluid-induced recrystallisation is a viable process that could have affected the geochronological record of Madagascar and therefore requires careful consideration in future studies. Our work also reveals the nature of the mineralising fluids that percolated Madagascan crust subsequent to the Ediacaran to early Cambrian metamorphism (CO_2-dominated fluid + dense SiO_2-rich colloid solution, later probably H_2O-rich fluid), adding to several previous studies that constrain the origin of mineralisation in this region (e.g. Morteani et al., 2013; Martin et al., 2014; Montel et al., 2018).

Declaration of competing interest

The authors declare that they have no known competing financial interests or personal relationships that could have appeared to influence the work reported in this paper.

Acknowledgments

We are grateful to Jean-Marie Boccard and Fréderic Arlaud for their help with sample preparation, Danijela Miletic Doric and Florian Duval are thanked for their assistance with ^{40}Ar/^{39}Ar dating, Chris Mark and David van Acken for their support during U−Pb dating and Agathe Martignier for her support with electron microscopy. Kalin Kouzmanov is gratefully acknowledged for several useful discussions about the inclusions that were encountered in the studied sample. We thank Simon Kelley for sharing the preliminary K−Ca dates of the same Itrongay feldspar crystal that was studied in Flude et al. (2014). Ian Parsons is acknowledged for providing a very helpful extended explanation for the transmission electron microscopy observations of Parsons and Lee (2005). We are grateful to Balz Kamber for handling our manuscript and to Igor Villa and Peter Reiners for their reviews. U−Pb isotopic analyses were carried out using equipment at the National Centre for Isotope Geochemistry (NCIG), Dublin, which is a joint venture of University College Dublin, Trinity College Dublin, University College Cork and National University of Ireland Galway, funded mainly by Science Foundation Ireland, including Grant No. 04/BR/ES0007/EC07 awarded to JSD. EB was supported by Science Foundation Ireland Grant No. 13/RC/2092, which is co-funded under the European Regional Development Fund, which also supported the purchase of the G2 laser. The ^{40}Ar/^{39}Ar facility at ISTO is supported by European Research Council advanced grant RHEOLITH (grant agreement no 290864), Agence Nationale de la Recherche projects LABEX VOLTAIRE (ANR-10-LABX-100-01) and EQUIPEX PLANEX (ANR-11-EQPX-0036), and Région Centre Val de Loire project ARGON. Funds for this project were awarded to RS by the Swiss National Science Foundation (200021_160052).

Appendix A. Supplementary data

Supplementary data to this article can be found online at https://doi.org/10.1016/j.chemgeo.2020.119841.

References

Ackermann, S., Kunz, M., Armbruster, T., 2004. Cation distribution in a Fe-bearing K-feldspar from Itrongay, Madagascar: a combined neutron- and X-ray single-crystal diffraction study. Schweiz. Mineral. Petrogr. Mitt. 84, 345–354. https://doi.org/10.5169/seals-63754.

Akizuki, M., Sunagawa, I., 1978. Study of the sector structure in adularia by means of optical microscopy, infra-red absorption, and electron microscopy. Mineral. Mag. 42, 453–462. https://doi.org/10.1180/minmag.1978.042.324.07.

Arnaud, N.O., Kelley, S.P., 1997. Argon behaviour in gem-quality orthoclase from Madagascar: experiments and some consequences for ^{40}Ar/^{39}Ar geochronology. Geochim. Cosmochim. Acta 61, 3227–3255. https://doi.org/10.1016/S0016-7037(97)00152-X.

Bakker, R.J., 2003. Package FLUIDS 1. Computer programs for analysis of fluid inclusion data and for modelling bulk fluid properties. Chem. Geol. 194, 3–23. https://doi.org/10.1016/S0009-2541(02)00268-1.

Baxter, E.F., 2010. Diffusion of noble gases in minerals. Rev. Mineral. Geochem. 72, 509–557. https://doi.org/10.2138/rmg.2010.72.11.

Behl, R.J., 2011. Chert spheroids of the Monterey Formation, California (USA): early-diagenetic structures of bedded siliceous deposits: Chert spheroids. Sedimentology 58, 325–351. https://doi.org/10.1111/j.1365-3091.2010.01165.x.

Bergemann, C., Gnos, E., Berger, A., Whitehouse, M., Mullis, J., Wehrens, P., Pettke, T., Janots, E., 2017. Th-Pb ion probe dating of zoned hydrothermal monazite and its implications for repeated shear zone activity: an example from the Central Alps, Switzerland: dating hydrothermal monazite, shear zones. Tectonics 36, 671–689. https://doi.org/10.1002/2016TC004407.

Berger, A., Gnos, E., Schreurs, G., Fernandez, A., Rakotondrazafy, M., 2006. Late Neoproterozoic, Ordovician and Carboniferous events recorded in monazites from southern-central Madagascar. Precambrian Res. 144, 278–296. https://doi.org/10.1016/j.precamres.2005.11.010.

Beyssac, O., Goffé, B., Chopin, C., Rouzaud, J.N., 2002. Raman spectra of carbonaceous

material in metasediments: a new geothermometer. J. Metamorph. Geol. 20, 859–871. https://doi.org/10.1046/j.1525-1314.2002.00408.x.
Cassata, W.S., Renne, P.R., 2013. Systematic variations of argon diffusion in feldspars and implications for thermochronometry. Geochim. Cosmochim. Acta 112, 251–287. https://doi.org/10.1016/j.gca.2013.02.030.
Černý, P., 1994. Evolution of feldspars in granitic pegmatites. In: Parsons, I. (Ed.), Feldspars and Their Reactions. Kluwer Academic Publishers, Dordrecht, pp. 501–540. https://doi.org/10.1007/978-94-011-1106-5_13.
Černý, P., Chapman, R., 1984. Paragenesis, chemistry and structural state of adularia from granitic pegmatites. Bull. Mineral. 107, 369–384. https://doi.org/10.3406/bulmi.1984.7767.
Černý, P., Chapman, R., 1986. Adularia from hydrothermal vein deposits; extremes in structural state. Can. Mineral. 24, 717–728.
Chafe, A.N., Villa, I.M., Hanchar, J.M., Wirth, R., 2014. A re-examination of petrogenesis and $^{40}Ar/^{39}Ar$ systematics in the Chain of Ponds K-feldspar:"diffusion domain" archetype versus polyphase hygrochronology. Contrib. Mineral. Petrol. 167, 1010. https://doi.org/10.1007/s00410-014-1010-x.
Chamberlain, K.R., Bowring, S.A., 2001. Apatite–feldspar U–Pb thermochronometer: a reliable, mid-range (450 °C), diffusion-controlled system. Chem. Geol. 172, 173–200. https://doi.org/10.1016/S0009-2541(00)00242-4.
Cherniak, D.J., 2010a. Diffusion in accessory minerals: zircon, titanite, apatite, monazite and xenotime. Rev. Mineral. Geochem. 72, 827–869. https://doi.org/10.2138/rmg.2010.72.18.
Cherniak, D.J., 2010b. Cation diffusion in feldspars. Rev. Mineral. Geochem. 72, 691–733. https://doi.org/10.2138/rmg.2010.72.15.
Cherniak, D.J., Watson, E.B., 2019. Ca diffusion in K-Feldspar. Lithos 348–349, 105200. https://doi.org/10.1016/j.lithos.2019.105200.
Chew, D.M., Sylvester, P.J., Tubrett, M.N., 2011. U–Pb and Th–Pb dating of apatite by LA-ICPMS. Chem. Geol. 280, 200–216. https://doi.org/10.1016/j.chemgeo.2010.11.010.
Chew, D.M., Petrus, J.A., Kamber, B.S., 2014. U–Pb LA–ICPMS dating using accessory mineral standards with variable common Pb. Chem. Geol. 363, 185–199. https://doi.org/10.1016/j.chemgeo.2013.11.006.
Cicconi, M.R., Neuville, D.R., 2019. Natural Glasses. In: Musgraves, J.D., Hu, J., Calvez, L. (Eds.), Springer Handbook of Glass. Springer International Publishing, Cham, pp. 771–812. https://doi.org/10.1007/978-3-319-93728-1_22.
Cochrane, R., Spikings, R.A., Chew, D., Wotzlaw, J.-F., Chiaradia, M., Tyrrell, S., Schaltegger, U., Van der Lelij, R., 2014. High temperature (> 350 °C) thermochronology and mechanisms of Pb loss in apatite. Geochim. Cosmochim. Acta 127, 39–56. https://doi.org/10.1016/j.gca.2013.11.028.
Collins, A.S., 2006. Madagascar and the amalgamation of central Gondwana. Gondwana Res. 9, 3–16. https://doi.org/10.1016/j.gr.2005.10.001.
Collins, A.S., Kinny, P.D., Razakamanana, T., 2012. Depositional age, provenance and metamorphic age of metasedimentary rocks from southern Madagascar. Gondwana Res. 21, 353–361. https://doi.org/10.1016/j.gr.2010.12.006.
Curtis, N.J., Gascooke, J.R., Johnston, M.R., Pring, A., 2019. A review of the classification of opal with reference to recent new localities. Minerals 9, 299. https://doi.org/10.3390/min9050299.
de Wit, M.J., Bowring, S.A., Ashwal, L.D., Randrianasolo, L.G., Morel, V.P.I., Rambeloson, R.A., 2001. Age and tectonic evolution of Neoproterozoic ductile shear zones in southwestern Madagascar, with implications for Gondwana studies. Tectonics 20, 1–45. https://doi.org/10.1029/2000TC900026.
Dodson, M.H., 1973. Closure temperature in cooling geochronological and petrological systems. Contrib. Mineral. Petrol. 40, 259–274. https://doi.org/10.1007/BF00373790.
Dohmen, R., Kasemann, S.A., Coogan, L., Chakraborty, S., 2010. Diffusion of Li in olivine. Part I: Experimental observations and a multi species diffusion model. Geochim. Cosmochim. Acta 74, 274–292. https://doi.org/10.1016/j.gca.2009.10.016.
Dong, G., Morrison, G.W., 1995. Adularia in epithermal veins, Queensland: morphology, structural state and origin. Mineral. Deposita 30, 11–19. https://doi.org/10.1007/BF00208872.
Duan, Z., Møller, N., Weare, J.H., 1992. Molecular dynamics simulation of PVT properties of geological fluids and a general equation of state of nonpolar and weakly polar gases up to 2000 K and 20,000 bar. Geochim. Cosmochim. Acta 56, 3839–3845. https://doi.org/10.1016/0016-7037(92)90175-I.
Duan, Z., Møller, N., Weare, J.H., 1996. A general equation of state for supercritical fluid mixtures and molecular dynamics simulation of mixture PVTX properties. Geochim. Cosmochim. Acta 60, 1209–1216. https://doi.org/10.1016/0016-7037(96)00004-X.
Emmel, B., Jacobs, J., Razakamanana, T., 2004. Titanite and apatite fission track analyses on basement rocks of central-southern Madagascar: constraints on exhumation and denudation rates along the eastern rift shoulder of the Morondava basin. J. Afr. Earth Sci. 38, 343–361. https://doi.org/10.1016/j.jafrearsci.2003.10.009.
Emmel, B., Jöns, N., Kröner, A., Jacobs, J., Wartho, J.-A., Schenk, V., Razakamanana, T., Austegard, A., 2008. From closure of the Mozambique Ocean to Gondwana breakup: new evidence from geochronological data of the Vohibory Terrane, southwest Madagascar. The Journal of Geology 116, 21–38. https://doi.org/10.1086/524121.
Emmel, B., Boger, S.D., Jacobs, J., Daszinnies, M.C., 2012. Maturity of central Madagascar's landscape — low-temperature thermochronological constraints. Gondwana Res. 21, 704–713. https://doi.org/10.1016/j.gr.2011.05.018.
Fernandez, A., Schreurs, G., Villa, I.M., Huber, S., Rakotondrazafy, M., 2003. Age constraints on the tectonic evolution of the Itremo region in central Madagascar. Precambrian Res. 123, 87–110. https://doi.org/10.1016/S0301-9268(03)00063-9.
Flude, S., Halton, A.M., Kelley, S.P., Sherlock, S.C., Schwanethal, J., Wilkinson, C.M., 2014. Observation of centimetre-scale argon diffusion in alkali feldspars: implications for $^{40}Ar/^{39}Ar$ thermochronology. Geol. Soc. Lond., Spec. Publ. 378, 265–275. https://doi.org/10.1144/SP378.25.
Frezzotti, M.L., Tecce, F., Casagli, A., 2012. Raman spectroscopy for fluid inclusion analysis. J. Geochem. Explor. 112, 1–20. https://doi.org/10.1016/j.gexplo.2011.09.009.
Giese, J., Berger, A., Schreurs, G., Gnos, E., 2011. The timing of the tectono-metamorphic evolution at the Neoproterozoic–Phanerozoic boundary in central southern Madagascar. Precambrian Res. 185, 131–148. https://doi.org/10.1016/j.precamres.2011.01.002.
Glorie, S., Jepson, G., Konopelko, D., Mirkamalov, R., Meeuws, F., Gilbert, S., Gillespie, J., Collins, A.S., Xiao, W., Dewaele, S., De Grave, J., 2019. Thermochronological and geochemical footprints of post-orogenic fluid alteration recorded in apatite: Implications for mineralisation in the Uzbek Tian Shan. Gondwana Res. 71, 1–15. doi:https://doi.org/10.1016/j.gr.2019.01.011.
Görz, H., Bhalla, R.J.R.S.B., White, E.W., 1970. Detailed cathodoluminescence characterization of common silicates, in: Weber, J.N., White, E. (Eds.), Space applications of Solid State Luminescent Phenomena. Pp. 62–70.
Götze, J., Krbetschek, M.R., Habermann, D., Wolf, D., 2000. High-resolution cathodoluminescence studies of feldspar minerals. In: Pagel, M., Barbin, V., Blanc, P., Ohnenstetter, D. (Eds.), Cathodoluminescence in Geosciences. Springer Berlin Heidelberg, Berlin, Heidelberg, pp. 245–270. https://doi.org/10.1007/978-3-662-04086-7_10.
Grégoire, V., Nédélec, A., Monié, P., Montel, J.-M., Ganne, J., Ralison, B., 2009. Structural reworking and heat transfer related to the late-Panafrican Angavo shear zone of Madagascar. Tectonophysics 477, 197–216. https://doi.org/10.1016/j.tecto.2009.03.009.
Hagen, E., Kelley, S.P., Dypvik, H., Nilsen, O., Kjølhamar, B., 2001. Direct dating of authigenic K-feldspar overgrowths from the Kilombero Rift of Tanzania. J. Geol. Soc. 158, 801–807. https://doi.org/10.1144/jgs.158.5.801.
Harrison, T.M., Lovera, O.M., 2014. The multi-diffusion domain model: past, present and future. Geol. Soc. Lond., Spec. Publ. 378, 91–106. https://doi.org/10.1144/SP378.9.
Holder, R.M., Hacker, B.R., 2019. Fluid-driven resetting of titanite following ultrahigh-temperature metamorphism in southern Madagascar. Chem. Geol. 504, 38–52. https://doi.org/10.1016/j.chemgeo.2018.11.017.
Holder, R.M., Hacker, B.R., Horton, F., Rakotondrazafy, A.F.M., 2018. Ultrahigh-temperature osumilite gneisses in southern Madagascar record combined heat advection and high rates of radiogenic heat production in a long-lived high- *T* orogen. J. Metamorph. Geol. 36, 855–880. https://doi.org/10.1111/jmg.12316.
Horton, F., Hacker, B., Kylander-Clark, A., Holder, R., Jöns, N., 2016. Focused radiogenic heating of middle crust caused ultrahigh temperatures in southern Madagascar. Tectonics 35, 293–314. https://doi.org/10.1002/2015TC004040.
Jackson, S.E., 2008. LAMTRACE data reduction software for LA-ICP-MS, in: Laser Ablation–ICP–MS in the Earth Sciences Current Practices and Outstanding Issues, Mineralogical Association of Canada Short Course Series. pp. 305–307.
Jöns, N., Schenk, V., 2011. The ultrahigh temperature granulites of southern Madagascar in a polymetamorphic context: implications for the amalgamation of the Gondwana supercontinent. Eur. J. Mineral. 23, 127–156. https://doi.org/10.1127/0935-1221/2011/0023-2087.
Kastner, M., Siever, R., 1979. Low temperature feldspars in sedimentary rocks. Am. J. Sci. 279, 435–479. https://doi.org/10.2475/ajs.279.4.435.
Keller, M.A., Isaacs, C.M., 1985. An evaluation of temperature scales for silica diagenesis in diatomaceous sequences including a new approach based on the Miocene Monterey Formation, California. Geo-Mar. Lett. 5, 31–35. https://doi.org/10.1007/BF02629794.
Khakimov, A.Kh, 1968. Genetic types of inclusions of agate amygdales and veins of the Idzhebanskii deposit in Armenia. In: Ermakov, N.P., Sobolev, V.S., Smirnov, V.I., Khitarov, N.I., Kuznetsov, V.A., Dolgov, Yu.A. (Eds.), Mineralogical Thermometry and Barometry. Volume II. New Methods and Results of Study of Parameters of Ore Formation. Nauka, Moscow, pp. 230–236.
Kirkland, C.L., Yakymchuk, C., Szilas, K., Evans, N., Hollis, J., McDonald, B., Gardiner, N.J., 2018. Apatite: a U-Pb thermochronometer or geochronometer? Lithos 318–319, 143–157. https://doi.org/10.1016/j.lithos.2018.08.007.
Koppers, A.A.P., 2002. ArArCALC—software for $^{40}Ar/^{39}Ar$ age calculations. Comput. Geosci. 28, 605–619. https://doi.org/10.1016/S0098-3004(01)00095-4.
Kotel'nikova, Z.A., Kotel'nikov, A.R., 2011. Na_2CO_3-bearing fluids: Experimental study at 700°C and under 1, 2, and 3 kbar pressure using synthetic fluid inclusions in quartz. Geology of Ore Deposits 53, 156–170. https://doi.org/10.1134/S1075701511020036.
Krainer, K., Spötl, C., 1989. Detrital and authigenic feldspars in Permian and early Triassic sandstones, Eastern Alps (Austria). Sediment. Geol. 62, 59–77. https://doi.org/10.1016/0037-0738(89)90101-2.
Kuiper, K.F., Deino, A., Hilgen, F.J., Krijgsman, W., Renne, P.R., Wijbrans, J.R., 2008. Synchronizing Rock Clocks of Earth history. Science 320, 500–504. https://doi.org/10.1126/science.1154339.
Lafuente, B., Downs, R.S., Yang, H., Stone, N., 2015. The power of databases: The RRUFF project. In: Armbruster, T., Danisi, R.M. (Eds.), Highlights in Mineralogical Crystallography. W. De Gruyter, Berlin, pp. 1–30. https://doi.org/10.1515/9783110417104-003.
Lamb, W.M., Valley, J.W., Brown, P.E., 1987. Post-metamorphic CO_2-rich fluid inclusions in granulites. Contrib. Mineral. Petrol. 96, 485–495. https://doi.org/10.1007/BF01166693.
Lamb, W.M., Brown, P.E., Valley, J.W., 1991. Fluid inclusions in Adirondack granulites: Implications for the retrograde P-T path. Contrib. Mineral. Petrol. 107, 472–483. https://doi.org/10.1007/BF00310681.
Lee, J.K.W., 1995. Multipath diffusion in geochronology. Contrib. Mineral. Petrol. 120, 60–82. https://doi.org/10.1007/BF00311008.
Lee, M.R., Parsons, I., 2003. Microtextures of authigenic Or-rich feldspar in the Upper Jurassic Humber Group, UK North Sea: Microtextures of authigenic feldspar.

Sedimentology 50, 597–608. https://doi.org/10.1046/j.1365-3091.2003.00567.x.
Lloyd, G.E., 1987. Atomic number and crystallographic contrast images with the SEM: a review of backscattered electron techniques. Mineral. Mag. 51, 3–19. https://doi.org/10.1180/minmag.1987.051.359.02.
London, D., Hunt, L.E., Schwing, C.R., Guttery, B.M., 2020. Feldspar thermometry in pegmatites: truth and consequences. Contrib. Mineral. Petrol. 175, 8. https://doi.org/10.1007/s00410-019-1617-z.
Lovera, O.M., Richter, F.M., Harrison, T.M., 1989. The $^{40}Ar/^{39}Ar$ thermochronometry for slowly cooled samples having a distribution of diffusion domain sizes. J. Geophys. Res. Solid Earth 94, 17917–17935. https://doi.org/10.1029/JB094iB12p17917.
Lovera, O.M., Grove, M., Harrison, T.M., 2002. Systematic analysis of K-feldspar $^{40}Ar/^{39}Ar$ step heating results II: Relevance of laboratory argon diffusion properties to nature. Geochim. Cosmochim. Acta 66, 1237–1255. https://doi.org/10.1016/S0016-7037(01)00846-8.
Lovera, O.M., Harrison, T.M., Boehnke, P., 2015. Comment on "Systematic variations of argon diffusion in feldspars and implications for thermochronometry" by Cassata and Renne. Geochim. Cosmochim. Acta 151, 168–171. https://doi.org/10.1016/j.gca.2014.11.016.
Mark, D.F., Parnell, J., Kelley, S.P., Sherlock, S.C., 2007. Resolution of regional fluid flow related to successive orogenic events on the Laurentian margin. Geology 35, 547. https://doi.org/10.1130/G23388A.1.
Markl, G., Bäuerle, J., Grujic, D., 2000. Metamorphic evolution of Pan-African granulite facies metapelites from Southern Madagascar. Precambrian Res. 102, 47–68. https://doi.org/10.1016/S0301-9268(99)00099-6.
Martelat, J.-E., Lardeaux, J.-M., Nicollet, C., Rakotondrazafy, R., 2000. Strain pattern and late Precambrian deformation history in southern Madagascar. Precambrian Res. 102, 1–20. https://doi.org/10.1016/S0301-9268(99)00083-2.
Martin, R.F., Randrianandraisana, A., Boulvais, P., 2014. Ampandrandava and similar phlogopite deposits in southern Madagascar: derivation from a silicocarbonatitic melt of crustal origin. J. Afr. Earth Sci. 94, 111–118. https://doi.org/10.1016/j.jafrearsci.2013.08.002.
McConnell, J.D.C., 1965. Electron optical study of effects associated with partial inversion in a silicate phase. The Philosophical Magazine: A Journal of Theoretical Experimental and Applied Physics 11, 1289–1301. https://doi.org/10.1080/14786436508224936.
Montel, J.-M., Razafimahatratra, D., de Parseval, P., Poitrasson, F., Moine, B., Seydoux-Guillaume, A.-M., Pik, R., Arnaud, N., Gibert, F., 2018. The giant monazite crystals from Manangotry (Madagascar). Chem. Geol. 484, 36–50. https://doi.org/10.1016/j.chemgeo.2017.10.034.
Morteani, G., Kostitsyn, Y.A., Gilg, H.A., Preinfalk, C., Razakamanana, T., 2013. Geochemistry of phlogopite, diopside, calcite, anhydrite and apatite pegmatites and syenites of southern Madagascar: evidence for crustal silicocarbonatitic (CSC) melt formation in a Panafrican collisional tectonic setting. Int. J. Earth Sci. 102, 627–645. https://doi.org/10.1007/s00531-012-0832-x.
Nägler, Th.F., Villa, I.M., 2000. In pursuit of the ^{40}K branching ratios: K-Ca and ^{39}Ar–^{40}Ar dating of gem silicates. Chem. Geol. 169, 5–16. https://doi.org/10.1016/S0009-2541(99)00194-1.
Nyfeler, D., Armbruster, T., Villa, I.M., 1998. Si, Al, Fe order-disorder in Fe-bearing K-feldspar from Madagascar and its implications to Ar diffusion. Schweiz. Mineral. Petrogr. Mitt. 78, 11–20. https://doi.org/10.5169/seals-59271.
Parsons, I., Lee, M.R., 2005. Minerals are not just chemical compounds. Can. Mineral. 43, 1959–1992. https://doi.org/10.2113/gscanmin.43.6.1959.
Parsons, I., Brown, W.L., Smith, J.V., 1999. $^{40}Ar/^{39}Ar$ thermochronology using alkali feldspars: real thermal history or mathematical mirage of microtexture? Contrib. Mineral. Petrol. 136, 92–110. https://doi.org/10.1007/s004100050526.
Parsons, I., Fitz Gerald, J.D., Lee, M.R., 2015. Routine characterization and interpretation of complex alkali feldspar intergrowths. Am. Mineral. 100, 1277–1303. https://doi.org/10.2138/am-2015-5094.
Paton, C., Hellstrom, J., Paul, B., Woodhead, J., Hergt, J., 2011. Iolite: Freeware for the visualisation and processing of mass spectrometric data. J. Anal. At. Spectrom. 26, 2508. https://doi.org/10.1039/c1ja10172b.
Paul, A.N., Spikings, R.A., Ulianov, A., Ovtcharova, M., 2018. High temperature (> 350 °C) thermal histories of the long lived (> 500 Ma) active margin of Ecuador and Colombia: Apatite, titanite and rutile U-Pb thermochronology. Geochim. Cosmochim. Acta 228, 275–300. https://doi.org/10.1016/j.gca.2018.02.033.
Paul, A.N., Spikings, R.A., Chew, D., Daly, J.S., 2019. The effect of intra-crystal uranium zonation on apatite U-Pb thermochronology: a combined ID-TIMS and LA-MC-ICP-MS study. Geochim. Cosmochim. Acta 251, 15–35. https://doi.org/10.1016/j.gca.2019.02.013.
Pearce, T., Kolisnik, A., 1990. Observations of plagioclase zoning using interference imaging. Earth Sci. Rev. 29, 9–26. https://doi.org/10.1016/0012-8252(0)90024-P.
Peretyazhko, I.S., Smirnov, S.Z., Kotel'nikov, A.R., Kotel'nikova, Z.A., 2010. Experimental study of the system H_3BO_3–NaF–SiO_2-H_2O at 350–800 °C and 1–2 kbar by the method of synthetic fluid inclusions. Russ. Geol. Geophys. 51, 349–368. https://doi.org/10.1016/j.rgg.2010.03.003.
Popov, D., Spikings, R., 2018. Closure temperature of apatite (U-Th-Pb system): effects of crystal geometry, parent isotope zonation, and petrological environment. Presented at the 16th International Conference on Thermochronology, Quedlinburg. Conference Abstracts, p. 160.
Popov, D.V., Spikings, R.A., 2020. Diffusion vs. fluid alteration in alkali feldspar $^{40}Ar/^{39}Ar$ thermochronology: does cross-correlation of $\log(r/r_0)$ and age spectra validate thermal histories? Chem. Geol. 539, 119506. https://doi.org/10.1016/j.chemgeo.2020.119506.
Popov, D.V., Spikings, R.A., Kouzmanov, K., 2020. Pathways for ^{39}Ar loss during step-heating of alkali feldspar megacrysts from the Shap granite (UK): combined evidence from diffusion experiments and characterisation of heating-induced texture modifications. Chem. Geol. https://doi.org/10.1016/j.chemgeo.2020.119677.
Rauchenstein-Martinek, K., 2014. Metamorphic fluid history along a cross section through the Central Alps: Constraints from LA-ICPMS analysis of fluid inclusions and Ar-Ar geochronology. (Doctoral dissertation). ETH. Zurich., 167. https://doi.org/10.3929/ethz-a-010342954.
Ricchi, E., Bergemann, C.A., Gnos, E., Berger, A., Rubatto, D., Whitehouse, M.J., 2019. Constraining deformation phases in the Aar Massif and the Gotthard Nappe (Switzerland) using Th-Pb crystallization ages of fissure monazite-(Ce). Lithos 342–343, 223–238. https://doi.org/10.1016/j.lithos.2019.04.014.
Robinson, V.N.E., 1980. Imaging with backscattered electrons in a scanning electron microscope. Scanning 3, 15–26. https://doi.org/10.1002/sca.4950030103.
Roedder, E., 1984. Fluid inclusions. Rev. Mineral. 12, 1–644.
Roig, J.-Y., Tucker, R.D., Peters, S.G., Delor, C., Théveniaut, H., 2012. Carte géologique de la République de Madagascar à 1/1000000.
Rossi, M., Rolland, Y., 2014. Stable isotope and Ar/Ar evidence of prolonged multiscale fluid flow during exhumation of orogenic crust: example from the Mont Blanc and Aar Massifs (NW Alps). Tectonics 33, 1681–1709. https://doi.org/10.1002/2013TC003438.
Saunders, J.A., 1994. Silica and gold textures in bonanza ores of the Sleeper Deposit, Humboldt County, Nevada; evidence for colloids and implications for epithermal ore-forming processes. Econ. Geol. 89, 628–638. https://doi.org/10.2113/gsecongeo.89.3.628.
Savornin, M.A., 1932. Madagascar, carte géologique de reconnaissance au 1/200000, coupure 585 Benenitra.
Savornin, M.A., 1933. Madagascar, carte géologique de reconnaissance au 1/200000, coupure 586 Betroka.
Scaillet, S., 2000. Numerical error analysis in $^{40}Ar/^{39}Ar$ dating. Chem. Geol. 162, 269–298. https://doi.org/10.1016/S0009-2541(99)00149-7.
Schoene, B., Bowring, S.A., 2006. U–Pb systematics of the McClure Mountain syenite: thermochronological constraints on the age of the $^{40}Ar/^{39}Ar$ standard MMhb. Contrib. Mineral. Petrol. 151, 615–630. https://doi.org/10.1007/s00410-006-0077-4.
Schoene, B., Bowring, S.A., 2007. Determining accurate temperature–time paths from U–Pb thermochronology: an example from the Kaapvaal craton, southern Africa. Geochim. Cosmochim. Acta 71, 165–185. https://doi.org/10.1016/j.gca.2006.08.029.
Seward, D., Grujic, D., Schreurs, G., 2004. An insight into the breakup of Gondwana: Identifying events through low-temperature thermochronology from the basement rocks of Madagascar. Tectonics 23, n/a-n/a. doi:https://doi.org/10.1029/2003TC001556.
Shcherbakov, V.D., Plechov, P.Yu., Izbekov, P.E., Shipman, J.S., 2011. Plagioclase zoning as an indicator of magma processes at Bezymianny Volcano, Kamchatka. Contrib. Mineral. Petrol. 162, 83–99. https://doi.org/10.1007/s00410-010-0584-1.
Simmons, W.B., Falster, A.U., 2002. Yellow Orthoclase (sanidine) from South Betroka, Madagascar. Mineral. Rec. 33, 79–80.
Simmons, Wm.B.S., Webber, K.L., 2008. Pegmatite genesis: state of the art. Eur. J. Mineral. 20, 421–438. https://doi.org/10.1127/0935-1221/2008/0020-1833.
Sirbescu, M.-L.C., Nabelek, P.I., 2003a. Crustal melts below 400 °C. Geology 31, 685. https://doi.org/10.1130/G19497.1.
Sirbescu, M.-L.C., Nabelek, P.I., 2003b. Crystallization conditions and evolution of magmatic fluids in the Harney Peak Granite and associated pegmatites, Black Hills, South Dakota—evidence from fluid inclusions. Geochim. Cosmochim. Acta 67, 2443–2465. https://doi.org/10.1016/S0016-7037(02)01408-4.
Smith, J.V., Stenstrom, R.C., 1965. Electron-Excited Luminescence as a Petrologic Tool. The Journal of Geology 73, 627–635. https://doi.org/10.1086/627098.
Stacey, J.S., Kramers, J.D., 1975. Approximation of terrestrial lead isotope evolution by a two-stage model. Earth Planet. Sci. Lett. 26, 207–221. https://doi.org/10.1016/0012-821X(75)90088-6.
Steiger, R.H., Jäger, E., 1977. Subcommission on geochronology: Convention on the use of decay constants in geo- and cosmochronology. Earth Planet. Sci. Lett. 36, 359–362. https://doi.org/10.1016/0012-821X(77)90060-7.
Takahashi, R., Müller, A., Matsueda, H., Okrugin, V.M., Ono, S., van den Kerkhof, A., Kronz, A., Andreeva, E.D., 2008. Cathodoluminescence and Trace Elements in Quartz : Clues to Metal Precipitation Mechanisms at the Asachinskoe Gold Deposit in Kamchatka. Presented at the International Symposium "The Origin and Evolution of Natural Diversity," Sapporo, Japan. pp. 175–184.
Thomas, R., Davidson, P., 2008. Water and melt/melt immiscibility, the essential components in the formation of pegmatites; evidence from melt inclusions. Z. Geol. Wiss. 36, 347–364.
Thomas, R., Davidson, P., 2012a. Water in granite and pegmatite-forming melts. Ore Geol. Rev. 46, 32–46. https://doi.org/10.1016/j.oregeorev.2012.02.006.
Thomas, R., Davidson, P., 2012b. Evidence of a water-rich silica gel state during the formation of a simple pegmatite. Mineral. Mag. 76, 2785–2801. https://doi.org/10.1180/minmag.2012.076.7.11.
Thomas, R., Webster, J.D., Heinrich, W., 2000. Melt inclusions in pegmatite quartz: complete miscibility between silicate melts and hydrous fluids at low pressure. Contrib. Mineral. Petrol. 139, 394–401. https://doi.org/10.1007/s004100000120.
Thomas, R., Davidson, P., Badanina, E., 2009. A melt and fluid inclusion assemblage in beryl from pegmatite in the Orlovka amazonite granite, East Transbaikalia, Russia: implications for pegmatite-forming melt systems. Mineral. Petrol. 96, 129–140. https://doi.org/10.1007/s00710-009-0053-6.
Touret, J., 1974. Faciès granulite et fluides carboniques. Annales de la Société géologique de Belgique. Publications spéciales, Géologie des domaines cristallins. Centenaire de la Société géologique de Belgique, pp. 267–287.
Touret, J., 1977. The significance of fluid inclusions in metamorphic rocks. In: Fraser, D.G. (Ed.), Thermodynamics in Geology. D. Reidel Publishing Company, Dordrecht,

pp. 203–227.
Touret, J.L.R., Huizenga, J.-M., 2011. Fluids in granulites. In: Origin and Evolution of Precambrian High-Grade Gneiss Terranes, With Special Emphasis on the Limpopo complex of Southern Africa. Geological Society of America. https://doi.org/10.1130/2011.1207(03.
Tsuchiyama, A., 1985. Dissolution kinetics of plagioclase in the melt of the system diopside-albite-anorthite, and origin of dusty plagioclase in andesites. Contrib. Mineral. Petrol. 89, 1–16. https://doi.org/10.1007/BF01177585.
Tsunogae, T., Santosh, M., Osanai, Y., Owada, M., Toyoshima, T., Hokada, T., 2002. Very high-density carbonic fluid inclusions in sapphirine-bearing granulites from Tonagh Island in the Archean Napier Complex, East Antarctica: implications for CO2 infiltration during ultrahigh-temperature (T > 1,100 °C) metamorphism. Contrib. Mineral. Petrol. 143, 279–299. https://doi.org/10.1007/s00410-001-0343-4.
Tucker, R.D., Roig, J.Y., Moine, B., Delor, C., Peters, S.G., 2014. A geological synthesis of the Precambrian shield in Madagascar. J. Afr. Earth Sci. 94, 9–30. https://doi.org/10.1016/j.jafrearsci.2014.02.001.
Ulianov, A., Müntener, O., Schaltegger, U., Bussy, F., 2012. The data treatment dependent variability of U–Pb zircon ages obtained using mono-collector, sector field, laser ablation ICPMS. J. Anal. At. Spectrom. 27, 663. https://doi.org/10.1039/c2ja10358c.
Villa, I.M., Hanchar, J.M., 2013. K-feldspar hygrochronology. Geochim. Cosmochim. Acta 101, 24–33. https://doi.org/10.1016/j.gca.2012.09.047.
Wartho, J.-A., Kelley, S.P., Brooker, R.A., Carroll, M.R., Villa, I.M., Lee, M.R., 1999. Direct measurement of Ar diffusion profiles in a gem-quality Madagascar K-feldspar using the ultra-violet laser ablation microprobe (UVLAMP). Earth Planet. Sci. Lett. 170, 141–153. https://doi.org/10.1016/S0012-821X(99)00088-6.
Wilkinson, J.J., Nolan, J., Rankin, A.H., 1996. Silicothermal fluid: a novel medium for mass transport in the lithosphere. Geology 24, 1059–1062. https://doi.org/10.1130/0091-7613(1996)024<1059:SFANMF>2.3.CO;2.
Worden, R.H., Rushton, J.C., 1992. Diagenetic K-feldspar textures: a TEM study and model for diagenetic feldspar growth. J. Sediment. Res. 62, 779–789. https://doi.org/10.1306/D42679D8-2B26-11D7-8648000102C1865D.